Structural and Multidisciplinary Optimization (2022) 65:129
https://doi.org/10.1007/s00158-022-03222-z

RESEARCH PAPER

Manufacturing and stiffness constraints for topology optimized periodic structures

Kenneth E. Swartz[1,2] · **Daniel A. Tortorelli**[1,2] · **Daniel A. White**[2] · **Kai A. James**[3]

Received: 13 October 2021 / Revised: 8 January 2022 / Accepted: 4 March 2022

Abstract
Topology optimization (TO) is commonly applied to design the unit cells of periodic structures. For example, metamaterials, lattice structures, phononic crystals (PhC), and photonic crystals (PC) have all been previously designed via TO. Unfortunately, the optimal structures for certain design objectives, e.g., bandgaps, are often impossible to manufacture as they have disconnected regions or "islands" of solid material (ISM) that are not self-supporting. Further, designs with enclosed void space (EVS) are problematic for additive manufacturing (AM) since support material or pre-sintered powder cannot be removed after manufacturing. We present a series of constraints that may be incorporated into any TO framework to ensure structures are self-supporting without enclosed voids. Additionally, we employ homogenization-based constraints that allow the designer to tune the elastic stiffness and isotropy of the optimized design. The proposed constraints are evaluated on example microstructures and utilized in a simple optimization test problem to highlight their abilities and limitations so that guidelines for appropriate combinations of constraints may be proposed. Effective constraint combinations are demonstrated on the design of 3D photonic crystals for maximum bandgap subject to manufacturing and stiffness constraints.

Keywords Topology optimization · Manufacturing constraints · Periodic structures · Metamaterials · Photonic crystals · Homogenization

1 Introduction

The design of periodic unit cells with inverse homogenization (Sigmund 1994) applies topology optimization (Bendsøe and Kikuchi 1988) to determine the optimal microstructure for a particular application. For example, it is used to design metamaterials with seemingly nonphysical effective properties, such as negative Poisson's ratio (Larsen et al. 1997; Babaee et al. 2013; Andreassen et al. 2014) and simultaneous negative bulk modulus and mass density (Ding et al. 2007). Inverse homogenization is also used to tune metamaterials to match prescribed properties (Sigmund 1995) and to obtain theoretically optimal properties (Sigmund 2000). The method is becoming more common in three dimensional (3D) applications (Andreassen et al. 2014) as computing power continues to advance, and the interest in lattice materials continues to grow (Messner 2016). Moreover, it is not limited to the realm of mechanics; designs for thermal expansion (Sigmund and Torquato 1996), thermal conductivity (de Kruijf et al. 2007), fluid permeability (Guest and Prévost 2007), and magnetic permeability (Diaz and Sigmund 2010) have also been generated, and multifunctional designs are becoming increasingly popular (Guest and Prevost 2006; de Kruijf et al. 2007). Interested readers are directed to an exhaustive review of micro-architected design (Osanov and Guest 2016).

Responsible Editor: Xiaojia Shelly Zhang

Topical Collection: 14th World Congress of Structural and Multidisciplinary Optimization Guest Editors: Y Noh, E Acar, J Carstensen, J Guest, J Norato, P Ramu.

✉ Kenneth E. Swartz
swartz10@llnl.gov

[1] Mechanical Science and Engineering, University of Illinois at Urbana-Champaign, 1206 W. Green St., Urbana, IL 61801, USA

[2] Computational Engineering Division, Lawrence Livermore National Laboratory, 7000 East Ave., Livermore, CA 94550, USA

[3] Aerospace Engineering, University of Illinois at Urbana-Champaign, 104 S. Wright St., Urbana, IL 61801, USA

Published online: 31 March 2022

Similar to inverse homogenization, topology optimization has been used to design the periodic unit cells of phononic and photonic crystals (Li et al. 2019). Early studies designed two-dimensional (2D) phononic (Sigmund and Jensen 2003) and photonic crystals (Kao et al. 2005; Men et al. 2010), and more recently 3D photonic crystals (Men et al. 2014; Meng et al. 2018; Swartz et al. 2021). Bandgap optimizations present an obvious need for material connectivity constraints. Indeed in stiffness optimizations, disconnected regions of material never appear as they increase mass but not stiffness. However, in bandgap optimization problems it has been demonstrated that disconnected structures are often beneficial (Kao et al. 2005; Men et al. 2010; Swartz et al. 2021). Such designs with islands of solid material (ISM) are problematic as they cannot be manufactured. Additionally, enclosed void space (EVS), also common to bandgap optimized designs (Men et al. 2014; Swartz et al. 2021), cannot be easily manufactured. Further, photonic crystals, as well as other periodic structures, require a minimum level of stiffness to operate properly. For example, an optics systems designed for a spacecraft would need to maintain its intended shape while subjected to both inertial loads and surface tractions. This will not be possible if the designs do not exhibit some requisite level of stiffness. Therefore, it is important to develop constraints that allow designers to tune the stiffness of periodic structures for their particular applications.

Many design formulations have been presented to ensure manufacturability in density-based topology optimization (Lazarov et al. 2016; Plocher and Panesar 2019). For example, techniques have been proposed to limit the overhang angle of a structure to alleviate the need for support material in additive manufacturing (AM) (Leary et al. 2014; Gaynor and Guest 2016; Qian 2016; Allaire et al. 2017; Liu and To 2017; Zhang et al. 2019); this topic has been intensely studied and is not the focus of this work. Previous work has used a mechanical eigenvalue constraint to avoid ISM in 2D periodic structures (Wang et al. 2011). We expand on this work by implementing a mechanical eigenvalue constraint for 3D periodic structures and point out a fundamental flaw in this constraint function. Effective thermal conductivity has also been used as a design constraint to enforce connected structures (Andreasen et al. 2014). We use a similar technique wherein we compute the effective stiffness tensor of the unit cell which allows us to constrain bulk stiffness, which behaves similarly to thermal conductivity, and/or shear stiffness. The capabilities and limitations of our effective property constraints are examined. Additionally, the virtual temperature method (VTM) (Liu et al. 2015) prevents EVS, which is difficult to manufacture with most AM processes. We present various constraints that can be integrated into topology optimization frameworks to ensure that optimal microstructures do not contain neither ISM nor EVS. Our techniques do not require changing the design parameterization or applying a filter. Further, since several of them are linked to mechanical stiffness we will investigate the effect of adding stiffness requirements to photonic bandgap structures. We will thus be able to generate manufacturable photonic crystal structures with prescribed levels of stiffness and probe the trade-off between these two often conflicting objectives.

We begin by extending the VTM (Liu et al. 2015) to prevent ISM by flipping the material properties in Sect. 2.1.1. Then, we further extend the VTM to eliminate both EVS and ISM from periodic structures in Sect. 2.1.2. We alternatively prevent ISM by enforcing a mechanical eigenvalue constraint described in Sect. 2.2 and ensure self-supporting structures by enforcing a self-weight compliance constraint described in Sect. 2.3. Finally, we compute the homogenized (Allaire 2002), or effective, constitutive tensor of our unit cells from which we derive bulk stiffness, shear stiffness, and isotropy constraints in Sect. 2.4. We highlight the novelty of our VTM extension for ISM prevention, the use of VTM with periodic structures, the extension of the mechanical eigenvalue constraint to three dimensions, and the development of the self-weight compliance constraint. Additionally, we present invariant bulk and shear modulus definitions that are easily differentiable making them amenable to inverse homogenization. The proposed constraints are quantitatively compared for a series of contrived unit cells to demonstrate their behavior in Sect. 3, where guidelines for the appropriate constraint choices are also presented to meet particular design goals. A simple optimization test problem is presented to display the efficacy of each constraint for unit cell design in Sect. 4. The optimal topologies obtained when using each design constraint are compared to demonstrate the behavior a designer can expect when using each function in a computational design framework. Self-supporting, manufacturable photonic crystals are designed for the first time to further exemplify the proposed constraints in Sect. 5. Finally, novel 3D photonic bandgap structures with prescribed minimum bulk stiffness levels are presented to illustrate a feasible bandgap-bulk stiffness design space in Sect. 6.

2 Constraint formulations

2.1 Virtual temperature method

The VTM (Liu et al. 2015), equivalently formulated as the virtual scalar field method (Li et al. 2016), was proposed as a technique to prevent EVS in topology optimized designs. A virtual "temperature" field is computed which satisfies the steady-state heat conduction equation

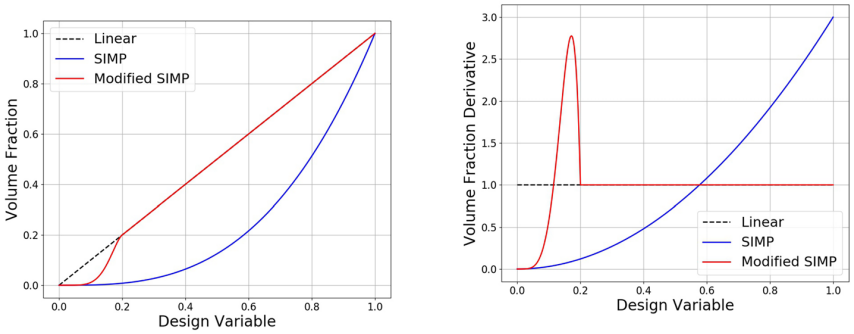

Fig. 1 A comparison of volume fraction interpolations

(a) Volume fraction interpolations

(b) Derivative of volume fraction interpolations

$$\begin{aligned} \nabla \cdot (k(\boldsymbol{x})\nabla T(\boldsymbol{x})) + Q(\boldsymbol{x}) = 0 \qquad & \text{for } \boldsymbol{x} \in \Omega \\ T(\boldsymbol{x}) = 0 \qquad & \text{for } \boldsymbol{x} \in \partial\Omega, \end{aligned} \tag{1}$$

where k is the conductivity, Q is a heat source, and T is the virtual temperature field at spatial coordinate $\boldsymbol{x}$. Although we are designing a periodic structure, the domain Ω considered for this constraint is just a few unit cells and we do not enforce periodic boundary conditions. This point is elaborated on in Sect. 2.1.2.

This technique works by placing the heat source and highly conductive material in the void phase, while placing insulating material and no heat source in the solid material. Thus, a much larger maximum domain temperature is observed when a region of void space is disconnected from the domain boundary $\partial\Omega$ since the heat is not be able to dissipate as it would if all of the void space was in contact with the boundary $\partial\Omega$. Specifically, the conductivity is computed as a function of the solid phase volume fraction $\phi \in [0, 1]$ according to a SIMP-like (Bendsøe 1989) interpolation

$$k(\phi) = \varepsilon k_0 + (1-\phi)^q \left(k_0 - \varepsilon k_0\right), \tag{2}$$

so that $k = k_0$ for $\phi = 0$ and $k = \varepsilon k_0$ for $\phi = 1$, i.e., we place highly conductive material k_0 in the $\phi = 0$ void phase and insulating material ($\varepsilon \ll 1$) in the $\phi = 1$ solid phase. We should note that these VTM material properties are not physical, e.g., we would not expect void space to be more conductive than solid material. For reasons below, we assign $q > 1$.

The heat source should only be present in the void phase and hence it is also a function of ϕ. However, it was observed in practice that using a linear interpolation, i.e., $Q(\phi) = (1-\phi)Q_0$ where Q_0 is the heat source value of the void phase, caused nonphysical behavior, e.g., negative temperatures, in regions with intermediate volume fraction. Fortunately, a modified SIMP interpolation scheme originally developed to remove spurious eigenmodes caused by low volume fraction elements (Du and Olhoff 2007) was able to resolve this issue. Figure 1 presents interpolations and their derivatives. We see that very low volume fractions are heavily penalized with the modified SIMP, but importantly the interpolation is C^1 continuous. We invert the modified SIMP interpolation so that the heat source in high volume fraction regions is penalized, i.e.,

$$Q(\phi) = \begin{cases} \left(c_1(1-\phi)^r + c_2(1-\phi)^{r+1}\right)Q_0 & \phi \geq \phi_{\mathrm{U}} \\ (1-\phi)Q_0 & \phi < \phi_{\mathrm{U}} \end{cases} \tag{3}$$

where $r > q$, ϕ_{U} is a volume fraction upper bound, and the constants c_1 and c_2 are selected to ensure the material interpolation scheme remains C^1 continuous. To enforce this continuity we require that both expressions in Eq. (3) produce the same value of $Q\left(\phi_{\mathrm{U}}\right)$ and $Q'\left(\phi_{\mathrm{U}}\right)$ from which we obtain

$$c_1 = r\left(1-\phi_{\mathrm{U}}\right)^{1-r} \tag{4}$$

and

$$c_2 = (1-r)\left(1-\phi_{\mathrm{U}}\right)^{-r}. \tag{5}$$

Note that for any choice of $\phi_{\mathrm{U}} \in (0, 1)$ we will obtain $Q = Q_0$ for $\phi = 0$ and $Q = 0$ for $\phi = 1$.

Selecting exponent values $q > 1$ serves to penalize intermediate volume fractions $\phi \in (0, 1)$ by reducing their conductivity-to-heat source ratios. This is directly analogous to the SIMP method for compliance minimization (Bendsøe 1989) wherein the stiffness of intermediate volume fraction material is disproportionately reduced relative to its mass so that optimal solutions contain only $\phi = 0$ or $\phi = 1$. Here, the conductivity of intermediate volume fraction material is disproportionately reduced relative to its heat source so that optimal solutions prefer $\phi = 0$ or $\phi = 1$, since the intermediate volume fraction is inefficient at lowering the domain temperature.

The boundary condition on $\partial\Omega$ allows heat to escape from Ω. Thus, EVS is easily identified by the presence of regions with high temperatures. We compute the maximum

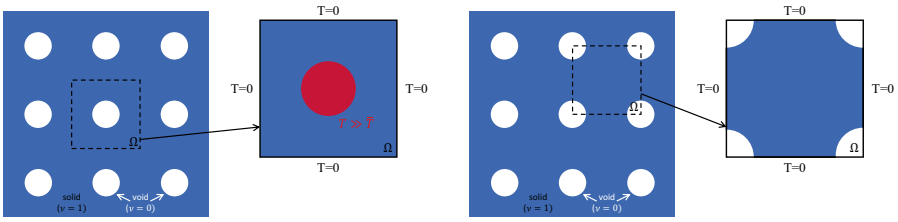

Fig. 2 Example behavior when a single unit cell is analyzed with VTM

(a) Example unit cell # 1 (b) Example unit cell # 2

temperature in the domain using the differentiable p-norm function

$$\theta_{\text{vt}} = \left(\int_{\Omega} T(\boldsymbol{x})^p \, \mathrm{d}\Omega \right)^{\frac{1}{p}}, \tag{6}$$

from which we formulate an optimization constraint as

$$\theta_{\text{vt}} \leq \mu_{\text{vt}} \bar{\theta}_{\text{vt}}, \tag{7}$$

where μ_{vt} is a user-specified parameter and $\bar{\theta}_{\text{vt}}$ is computed by Eq. (6) after solving Eq. (1) with $\phi(\boldsymbol{x}) = 0$ for all $\boldsymbol{x} \in \Omega$ so that the constraint limit is not problem dependent.

Henceforth we will use the subscript *vtv* when Eq. (7) is applied with the conductive material and heat source placed in the void phase as described above, and we will use the subscript *vts* when Eq. (7) is applied with the conductive material and heat source placed in the solid material as described in Sect. 2.1.1.

2.1.1 Extending the VTM to identify ISM

The VTM presented in Sect. 2.1 provides a quantitative means of identifying and preventing EVS. We propose a simple extension of this method to identify and prevent ISM. By simply inverting the interpolations in Eqs. (2) and (3) to

$$k(\phi) = \varepsilon k_0 + \phi^q \left(k_0 - \varepsilon k_0 \right) \tag{8}$$

and

$$Q(\phi) = \begin{cases} \left(c_1 \phi^r + c_2 \phi^{r+1} \right) Q_0 & \phi \leq \phi_{\text{L}} \\ \phi Q_0 & \phi > \phi_{\text{L}} \end{cases} \tag{9}$$

respectively, we place the conductive material and heat source in the solid rather than the void region. Repeating our continuity requirements we obtain

$$c_1 = r \phi_{\text{L}}^{1-r} \tag{10}$$

and

$$c_2 = (1 - r) \phi_{\text{L}}^{-r}. \tag{11}$$

In this way the maximum temperature will be large when we have regions of solid material not connected to a boundary. We can simultaneously restrict EVS and ISM by solving Eq. (1) twice; once using Eqs. (2) and (3) and again using Eqs. (8) and (9) and constraining the maximum temperature of each field via Eq. (7).

2.1.2 Extending to periodic domains

To the authors' knowledge the VTM has thus far only been applied to finite domains, although the effect of different boundary conditions has been explored (Li et al. 2018). We propose a technique to use VTM to prevent EVS and ISM in periodic structures. Consider a 2D microstructure consisting of solid material and a square array of circular voids. If we apply the VTM to the unit cell pictured in Fig. 2a, we would identify EVS. However, if we apply the VTM to the unit cell pictured in Fig. 2b, we will not identify EVS even though both unit cells represent the same periodic structure. Thus, we have an unacceptable problem; the behavior of our constraint function depends on the unit cell choice. To resolve this issue, we simply consider a 2^d array of unit cells, where d is the spatial dimension of our design problem. Indeed, consider the unit cell arrays highlighted in Fig. 3a and b. Although the number of "hot" (denoted by red) regions will be different, the behavior of the constraint will be consistent, i.e., EVS will be identified in either case. In fact, any valid array of 2^d unit cells will allow the VTM to appropriately identify EVS and ISM. We note that it would be preferable to compute the virtual temperature field over a single unit cell with periodic boundary conditions, but this presents a problem. Essential boundary conditions of $T = 0$ are required to dissipate the heat source and obtain the desired constraint behavior when the void space is not enclosed. However, if we place periodic boundary conditions on the exterior of our domain we do not know where to place the essential boundary condition because the location of solid/void space is not known *a priori*. Indeed, arbitrarily defining this essential boundary condition region would have the undesirable effect of dictating the resulting optimized design.

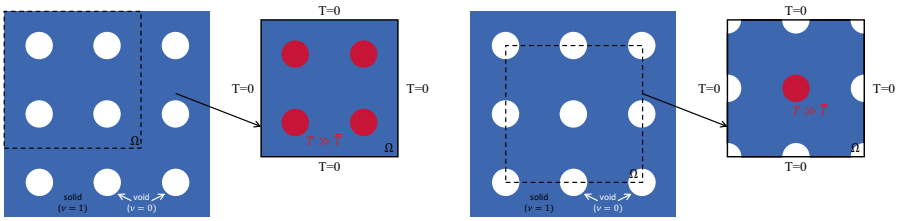

Fig. 3 Example behavior when a 2^2 unit cell array is analyzed with VTM

(a) Example unit cell array # 1 (b) Example unit cell array # 2

2.1.3 Sensitivity analysis

We must compute the sensitivities of our constraint functions with respect to design variables to solve our design optimization problem via nonlinear programming (NLP). Here we derive the sensitivities of our constraint functions with respect to the volume fraction field ϕ. However, we emphasize that other design parameterizations could be employed, e.g., projection methods (Watts and Tortorelli 2017) or B-splines (Qian 2013).

We evaluate the variation of Eq. (6) to obtain

$$\delta\theta_{\text{vt}} = \left(\int_\Omega T(\boldsymbol{x})^p \,\mathrm{d}\Omega\right)^{\frac{1}{p}-1} \int_\Omega T(\boldsymbol{x})^{p-1}\delta T(\boldsymbol{x}) \,\mathrm{d}\Omega, \tag{12}$$

where we notice the implicit sensitivity δT is problematic to compute analytically. We use the adjoint method to address this issue wherein we restate Eq. (1) in its weak form, i.e., we find $T \in \mathcal{H} = \{T \in H^1; T = 0 \text{ on } \partial\Omega\}$ for an H^1 Hilbert space such that

$$-\int_\Omega \nabla w(\boldsymbol{x}) \cdot k(\boldsymbol{x}) \nabla T(\boldsymbol{x}) \,\mathrm{d}\Omega + \int_\Omega w(\boldsymbol{x}) Q(\boldsymbol{x}) = 0 \tag{13}$$

for all $w \in \mathcal{H}$. Differentiating the above gives the problem of finding $\delta T \in \mathcal{H}$ satisfying

$$\begin{aligned} &-\int_\Omega \nabla w(\boldsymbol{x}) \cdot \delta k(\boldsymbol{x}) \nabla T(\boldsymbol{x}) \,\mathrm{d}\Omega - \int_\Omega \nabla w(\boldsymbol{x}) \cdot k(\boldsymbol{x}) \nabla \delta T(\boldsymbol{x}) \,\mathrm{d}\Omega \\ &+ \int_\Omega w(\boldsymbol{x}) \delta Q(\boldsymbol{x}) \,\mathrm{d}\Omega = 0 \end{aligned} \tag{14}$$

for all $w \in \mathcal{H}$. We now add Eq. (14), i.e., zero, to Eq. (12) to obtain

$$\begin{aligned} \delta\theta_{\text{vt}} = &\left(\int_\Omega T(\boldsymbol{x})^p \,\mathrm{d}\Omega\right)^{\frac{1}{p}-1} \int_\Omega T(\boldsymbol{x})^{p-1}\delta T(\boldsymbol{x}) \,\mathrm{d}\Omega \\ &- \int_\Omega \nabla w(\boldsymbol{x}) \cdot \delta k(\boldsymbol{x}) \nabla T(\boldsymbol{x}) \,\mathrm{d}\Omega \\ &- \int_\Omega \nabla w(\boldsymbol{x}) \cdot k(\boldsymbol{x}) \nabla \delta T(\boldsymbol{x}) \,\mathrm{d}\Omega + \int_\Omega w(\boldsymbol{x}) \delta Q(\boldsymbol{x}) \,\mathrm{d}\Omega, \end{aligned} \tag{15}$$

and notice that upon solving for $w \in \mathcal{H}$ such that

$$\int_\Omega \nabla \delta T(\boldsymbol{x}) \cdot k(\boldsymbol{x}) \nabla w(\boldsymbol{x}) \,\mathrm{d}\Omega = \left(\int_\Omega T(\boldsymbol{x})^p \,\mathrm{d}\Omega\right)^{\frac{1}{p}-1} \int_\Omega \delta T(\boldsymbol{x}) T(\boldsymbol{x})^{p-1} \,\mathrm{d}\Omega \tag{16}$$

for all $\delta T \in \mathcal{H}$ we can remove δT from Eq. (15). Subsequently substituting this w into Eq. (15) yields

$$\delta\theta_{\text{vt}} = -\int_\Omega \nabla w(\boldsymbol{x}) \cdot \delta k(\boldsymbol{x}) \nabla T(\boldsymbol{x}) \,\mathrm{d}\Omega + \int_\Omega w(\boldsymbol{x}) \delta Q(\boldsymbol{x}) \,\mathrm{d}\Omega. \tag{17}$$

We parameterize ϕ to be piece-wise uniform over the finite element mesh, i.e., each finite element Ω_i in Ω is assigned a distinct volume fraction ϕ_i. As such

$$\frac{\mathrm{D}\theta_{\text{vt}}}{\mathrm{D}\phi_i} = -\int_{\Omega_i} \nabla w(\boldsymbol{x}) \cdot \frac{\mathrm{D}k(\boldsymbol{x})}{\mathrm{D}\phi_i} \nabla T(\boldsymbol{x}) \,\mathrm{d}\Omega + \int_{\Omega_i} w(\boldsymbol{x}) \frac{\mathrm{D}Q(\boldsymbol{x})}{\mathrm{D}\phi_i} \,\mathrm{d}\Omega, \tag{18}$$

where we note that

$$\frac{\mathrm{D}k}{\mathrm{D}\phi_i} = -q\left(1-\phi_i\right)^{q-1}\left(k_0 - \varepsilon k_0\right) \tag{19}$$

and

$$\frac{\mathrm{D}Q}{\mathrm{D}\phi_i} = \begin{cases} \left(-c_1 q\left(1-\phi_i\right)^{r-1} - c_2(r+1)\left(1-\phi_i\right)^r\right)Q_0 & \phi_i \geq \phi_{\text{U}} \\ -Q_0 & \phi_i < \phi_{\text{U}} \end{cases} \tag{20}$$

when using the interpolation schemes in Eqs. (2) and (3), i.e., when restricting EVS. Similarly,

$$\frac{\mathrm{D}k}{\mathrm{D}\phi_i} = q\phi_i^{q-1}\left(k_0 - \varepsilon k_0\right) \tag{21}$$

and

$$\frac{\mathrm{D}Q}{\mathrm{D}\phi_i} = \begin{cases} \left(c_1 r\phi^{r-1} + c_2(q+1)\phi^r\right)Q_0 & \phi_i \leq \phi_{\text{L}} \\ Q_0 & \phi_i > \phi_{\text{L}} \end{cases} \tag{22}$$

when using the interpolation schemes in Eqs. (8) and (9), i.e., when restricting ISM.

2.2 Mechanical eigenvalues

Another constraint that identifies ISM is derived from an eigenvalue analysis that consists of solving for eigenpairs $(\lambda_j, \boldsymbol{u}_j)$ ordered such that $\lambda_1 \leq \lambda_2 \leq ... \leq \lambda_n$ that satisfy

$$\begin{aligned} \nabla \cdot \mathbb{C}(\boldsymbol{x})\big[\nabla \boldsymbol{u}_j(\boldsymbol{x})\big] &= \lambda_j \rho(\boldsymbol{x}) \boldsymbol{u}_j(\boldsymbol{x}) \quad && \text{for } \boldsymbol{x} \in \Omega \\ \boldsymbol{u}_j(\boldsymbol{x}) &= \boldsymbol{u}_j(\boldsymbol{x} + n\boldsymbol{a}_k) && \text{for } n = \mathbb{Z}, \end{aligned} \tag{23}$$

where $\mathbb{C}$ is the fourth-order elasticity tensor, ρ is the mass density, $\boldsymbol{u}$ is the displacement, Ω is a periodic domain, i.e., a unit cell, $\mathbb{Z}$ is the set of all integers, and $\boldsymbol{a}_k$ are the lattice vectors. Thus, we are employing periodic boundary conditions to appropriately model the response of our infinitely periodic structure. We use the SIMP interpolation (Bendsøe 1989) for the constitutive tensor according to

$$\mathbb{C}(\phi) = \varepsilon \mathbb{C}_0 + \phi^q \big(\mathbb{C}_0 - \varepsilon \mathbb{C}_0\big), \tag{24}$$

so that we place a stiff material in the solid phase, i.e., $\mathbb{C}(1) = \mathbb{C}_0$ and a weak material in the void phase, i.e., $\mathbb{C}(0) = \varepsilon \mathbb{C}_0$, where $\mathbb{C}_0$ is the elasticity tensor of the solid material. We use the modified SIMP (Du and Olhoff 2007) to interpolate the mass density according to

$$\rho(\phi) = \begin{cases} \big(c_1 \phi^r + c_2 \phi^{r+1}\big)\rho_0 & \phi \leq \phi_{\mathrm{L}} \\ \phi \rho_0 & \phi > \phi_{\mathrm{L}} \end{cases}, \tag{25}$$

wherein c_1 and c_2 are given in Eqs. (10) and (11), respectively.

We know that $\lambda_j \geq 0$ since the left-hand side operator in Eq. (23) is positive semi-definite, and we expect 3 zero-valued eigenvalues corresponding to rigid translation, i.e., $\lambda_1 = \lambda_2 = \lambda_3 = 0$. We show in Sect. 3 that we can identify ISM by observing the magnitude of the fourth-smallest eigenvalue. There will be nearly zero-valued eigenvalues λ_j for $j = 4, 5, \ldots, n$ when ISM are present, where the lower limit of λ_4 is determined by the selection of ε. As such, we estimate the fourth-smallest eigenvalue using a p-norm function

$$\theta_{\mathrm{eig}} = \left(\sum_{i=4}^{n} \lambda_i^{-p} \right)^{-\frac{1}{p}}, \tag{26}$$

and subsequently enforce the optimization constraint

$$\theta_{\mathrm{eig}} \geq \mu_{\mathrm{eig}} \bar{\theta}_{\mathrm{eig}}, \tag{27}$$

where μ_{eig} is a user-specified parameter and $\bar{\theta}_{\mathrm{eig}}$ is computed from Eq. (26) with the entire domain set to $\phi = 1$. We use Eq. (26) rather than $\theta_{\mathrm{eig}} = \lambda_4$ since Eq. (26) is differentiable even if λ_4 is a degenerate eigenvalue, i.e., even if $\lambda_4 = \lambda_5 \leq ... \leq \lambda_n$. We necessarily have $\lambda_3 < \lambda_4$ due to the ersatz material usage and therefore Eq. (26) is a symmetric polynomial of a distinct set of eigenvalues and hence differentiable (Gravesen et al. 2011). We do not use essential boundary conditions to constrain the rigid body translation modes for the reason discussed in Sect. 2.1.2. This issue is also discussed in a previous study (Andreasen et al. 2014).

We compute the sensitivity of the eigenvalues λ^j according to

$$\begin{aligned} \delta \lambda_j = \left(\int_\Omega \boldsymbol{u}_j(\boldsymbol{x}) \cdot \rho(\boldsymbol{x}) \boldsymbol{u}_j(\boldsymbol{x}) \mathrm{d}\Omega \right)^{-1} \Bigg(& \int_\Omega \nabla \boldsymbol{u}_j(\boldsymbol{x}) \cdot \delta \mathbb{C}(\boldsymbol{x}) \big[\nabla \boldsymbol{u}_j(\boldsymbol{x})\big] \mathrm{d}\Omega \\ & - \lambda_j \int_\Omega \boldsymbol{u}_j(\boldsymbol{x}) \cdot \delta \rho(\boldsymbol{x}) \boldsymbol{u}_j(\boldsymbol{x}) \mathrm{d}\Omega \Bigg). \end{aligned} \tag{28}$$

For our discretization this gives

$$\begin{aligned} \frac{\mathrm{D}\lambda_j}{\mathrm{D}\phi_i} = \left(\int_\Omega \boldsymbol{u}_j(\boldsymbol{x}) \cdot \rho(\boldsymbol{x}) \boldsymbol{u}_j(\boldsymbol{x}) \mathrm{d}\Omega \right)^{-1} \Bigg(& \int_{\Omega_i} \nabla \boldsymbol{u}_j(\boldsymbol{x}) \cdot \frac{\mathrm{D}\mathbb{C}(\boldsymbol{x})}{\mathrm{D}\phi_i} \big[\nabla \boldsymbol{u}_j(\boldsymbol{x})\big] \mathrm{d}\Omega \\ & - \lambda_j \int_{\Omega_i} \boldsymbol{u}_j(\boldsymbol{x}) \cdot \frac{\mathrm{D}\rho(\boldsymbol{x})}{\mathrm{D}\phi_i} \boldsymbol{u}_j(\boldsymbol{x}) \mathrm{d}\Omega \Bigg). \end{aligned} \tag{29}$$

where

$$\frac{\mathrm{D}\mathbb{C}}{\mathrm{D}\phi_i} = q \phi_i^{q-1} \big(\mathbb{C}_0 - \varepsilon \mathbb{C}_0\big) \tag{30}$$

and

$$\frac{\mathrm{D}\rho}{\mathrm{D}\phi_i} = \begin{cases} \big(c_1 r \phi_i^{r-1} + c_2 (r+1) \phi_i^r\big)\rho_0 & \phi_i \leq \phi_{\mathrm{L}} \\ \rho_0 & \phi_i > \phi_{\mathrm{L}} \end{cases}. \tag{31}$$

The derivative of Eq. (26) is computed as

$$\frac{\mathrm{D}\theta_{\mathrm{eig}}}{\mathrm{D}\lambda_j} = \left(\sum_{i=4}^{M} \lambda_i^{-p} \right)^{-\frac{1}{p}-1} \left(\lambda_j^{-p-1} \right). \tag{32}$$

and the derivative $\frac{\mathrm{D}\theta_{\mathrm{eig}}}{\mathrm{D}\phi_i}$ follows from an application of the chain rule.

2.3 Self-weight compliance

The periodic VTM presented above is very effective at identifying ISM and EVS. We will see in Sect. 3, however, a lack of ISM does not guarantee a structure is self-supporting. Thus, we propose a self-weight compliance constraint to ensure the unit cell is adequately supported. To do this we solve for the displacements $\boldsymbol{u}_i$ resulting from design-dependent body loads in each spatial dimension $\boldsymbol{e}_i$ according to

$$\begin{aligned} \nabla \cdot \mathbb{C}(\boldsymbol{x})\big[\nabla \boldsymbol{u}_i(\boldsymbol{x})\big] + \rho(\boldsymbol{x}) \boldsymbol{e}_i &= 0 \quad && \text{for } \boldsymbol{x} \in \Omega \\ \boldsymbol{u}_i(\boldsymbol{x}) &= 0 && \text{for } \boldsymbol{x} \in \Gamma_i, \end{aligned} \tag{33}$$

where the domain Ω is a single unit cell. The unit cell is not subject to periodic boundary conditions, but rather zero

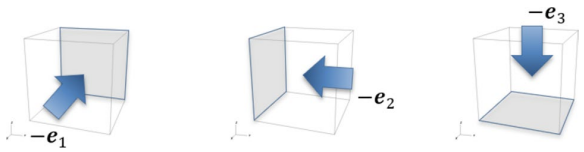

Fig. 4 Locations (in gray) of essential boundary conditions when computing θ_{swc}

displacement boundary conditions applied to Γ_i. We define Γ_i as the face that is "below" the unit cell, i.e., the face with an outward normal vector of $-\boldsymbol{e}_i$ where $\boldsymbol{e}_i$ is a canonical basis vector, cf. Fig. 4. We again use SIMP (Bendsøe 1989) to interpolate the constitutive tensor from Eq. (24) and the modified SIMP (Du and Olhoff 2007) to interpolate the mass density from Eq. (25). After evaluating the displacements $\boldsymbol{u}_i$, we evaluate the mean compliance

$$\theta_{\text{swc}} = -\sum_{i=1}^{3} \int_{\Omega} \rho(\boldsymbol{x}) \boldsymbol{e}_i \cdot \boldsymbol{u}_i(\boldsymbol{x}) \mathrm{d}\Omega. \tag{34}$$

The value of θ_{swc} will be small when the structure is fully supported, otherwise it will be very large. Knowing this we enforce the self-weight compliance constraint

$$\theta_{\text{swc}} \leq \mu_{\text{swc}} \bar{\theta}_{\text{swc}}, \tag{35}$$

where μ_{swc} is a user-specified parameter and $\bar{\theta}_{\text{swc}}$ is computed by Eq. (34) with $\phi = 1$ prescribed on the entire domain.

The sensitivity of θ_{swc} is obtained via the adjoint method (Bendsøe and Sigmund 2004) as

$$\begin{aligned} \delta\theta_{\text{swc}} = &-2 \sum_{i=1}^{3} \int_{\Omega} \delta\rho(\boldsymbol{x}) \boldsymbol{e}_i \cdot \boldsymbol{u}_i(\boldsymbol{x}) \mathrm{d}\Omega \\ &- \sum_{i=1}^{3} \int_{\Omega} \nabla \boldsymbol{u}_i(\boldsymbol{x}) \cdot \delta\mathbb{C}(\boldsymbol{x}) \left[\nabla \boldsymbol{u}_i(\boldsymbol{x})\right] \mathrm{d}\Omega, \end{aligned} \tag{36}$$

from which we obtain

$$\begin{aligned} \frac{\mathrm{D}\theta_{\text{swc}}}{\mathrm{D}\phi_i} = &-2 \sum_{i=1}^{3} \int_{\Omega_i} \frac{\mathrm{D}\rho(\boldsymbol{x})}{\mathrm{D}\phi_i} \boldsymbol{e}_i \cdot \boldsymbol{u}_i(\boldsymbol{x}) \mathrm{d}\Omega \\ &- \sum_{i=1}^{3} \int_{\Omega_i} \nabla \boldsymbol{u}_i(\boldsymbol{x}) \cdot \frac{\mathrm{D}\mathbb{C}(\boldsymbol{x})}{\mathrm{D}\phi_i} \left[\nabla \boldsymbol{u}_i(\boldsymbol{x})\right] \mathrm{d}\Omega. \end{aligned} \tag{37}$$

where $\frac{\mathrm{D}\mathbb{C}}{\mathrm{D}\phi_i}$ and $\frac{\mathrm{D}\rho}{\mathrm{D}\phi_i}$ follow from Eqs. (30) and (31).

Note that we must again consider an array of 2^d unit cells to ensure that our choice of unit cell does not affect the intent of the constraint function, cf. Fig. 3. In our numerical examples, however, we will only consider a single unit cell due to the imposed orthorhombic symmetry on the unit cell which eliminates the constraint's dependence on the cell. Unfortunately, this simplification is not possible with the VTM.

2.4 Effective stiffness constraints

In addition to the previously discussed EVS, ISM, and self-supporting constraints, we investigate constraints derived from the effective stiffness of our unit cell. Following classical homogenization theory (Allaire 2002), we first solve a series of unit cell problems for the characteristic displacements $\boldsymbol{\chi}^{ij}$

$$\begin{aligned} \nabla \cdot \mathbb{C}(\boldsymbol{x}) \left[\boldsymbol{E}^{ij} + \nabla \boldsymbol{\chi}^{ij}(\boldsymbol{x})\right] &= 0 \text{ for } \boldsymbol{x} \in \Omega \\ \boldsymbol{u}_i(\boldsymbol{x}) &= \boldsymbol{u}_i(\boldsymbol{x} + n\boldsymbol{a}_k) \text{ for } n = \mathbb{Z}, \end{aligned} \tag{38}$$

where $\boldsymbol{E}^{ij} \equiv \boldsymbol{e}^i \otimes \boldsymbol{e}^j$ is a unit "test" strain and Ω is the unit cell subject to periodic boundary conditions, c.f. Eq. (23). Upon obtaining each unique $\boldsymbol{\chi}^{ij}$, i.e., 6 displacement solutions in 3D, the components of the homogenized stiffness tensor $\mathbb{C}^{\text{h}}$ are computed according to

$$\mathbb{C}^{\text{h}}_{ijkl} = \frac{1}{|\Omega|} \int_{\Omega} \boldsymbol{E}^{ij} \cdot \mathbb{C}(\boldsymbol{x}) \left[\boldsymbol{E}^{kl} + \nabla \boldsymbol{\chi}^{kl}(\boldsymbol{x})\right] \mathrm{d}\Omega, \tag{39}$$

where $|\Omega|$ is the volume of the unit cell. We evaluate the design sensitivity of $\mathbb{C}^{\text{h}}$ using the adjoint technique (Allaire 2002; Watts and Tortorelli 2016) according to

$$\delta\mathbb{C}^{\text{h}}_{ijkl} = \frac{1}{|\Omega|} \int_{\Omega} \left(\boldsymbol{E}^{ij} + \nabla \boldsymbol{\chi}^{ij}(\boldsymbol{x})\right) \cdot \delta\mathbb{C}(\boldsymbol{x}) \left[\boldsymbol{E}^{kl} + \nabla \boldsymbol{\chi}^{kl}(\boldsymbol{x})\right] \mathrm{d}\Omega. \tag{40}$$

The interpolation of $\mathbb{C}$ from Eq. (24), and therefore the derivative in Eq. (30), are again used here. We investigate a number of constraint functions that depend explicitly on the components of $\mathbb{C}^{\text{h}}$.

2.4.1 Bulk modulus

The bulk modulus measures the volume change due to a uniform pressure loading. We express the bulk modulus as a function of the homogenized stiffness tensor according to

$$\kappa(\mathbb{C}) = \frac{1}{\boldsymbol{I} \cdot \mathbb{C}^{-1}[\boldsymbol{I}]}, \tag{41}$$

noting that we drop the superscript h for brevity and $\boldsymbol{I}$ is the identity 2-tensor that represents a unit hydrostatic pressure. The derivative of the bulk modulus with respect to a component of $\mathbb{C}$ is computed as

$$\frac{\mathrm{D}\kappa(\mathbb{C})}{\mathrm{D}\mathbb{C}_{ijkl}} = \frac{1}{\left(\boldsymbol{I} \cdot \mathbb{C}^{-1}[\boldsymbol{I}]\right)^2} \left(\boldsymbol{I} \cdot \left(\mathbb{C}^{-1} \frac{\mathrm{D}\mathbb{C}}{\mathrm{D}\mathbb{C}_{ijkl}} \mathbb{C}^{-1}\right)[\boldsymbol{I}]\right). \tag{42}$$

Following our previous conventions we define the bulk modulus constraint

$$\kappa \geq \mu_\kappa \bar{\kappa}, \tag{43}$$

where μ_κ is a user-specified parameter and $\bar{\kappa}$ is computed by prescribing $\phi = 1$ throughout the domain, or equivalently computed for an isotropic solid constituent material from its Young's modulus E and Poisson's ratio ν as $\bar{\kappa} = \frac{E}{3(1-2\nu)}$.

2.4.2 Shear modulus

We will define a shear modulus that is analogous to our bulk modulus definition in Eq. (41). To quantify shear stiffness we define a shear stress tensor

$$\boldsymbol{S} = \frac{1}{\sqrt{3}}\begin{bmatrix} 0 & 1 & 1 \\ 1 & 0 & 1 \\ 1 & 1 & 0 \end{bmatrix} \tag{44}$$

and express a "mean" shear modulus

$$\gamma(\mathbb{C}) = \frac{1}{\boldsymbol{S} \cdot \mathbb{C}^{-1}[\boldsymbol{S}]}. \tag{45}$$

The derivative of the shear modulus with respect to a component of $\mathbb{C}$ is computed from Eq. (43) with $\boldsymbol{S}$ replacing $\boldsymbol{I}$, i.e.,

$$\frac{\mathrm{D}\gamma(\mathbb{C})}{\mathrm{D}\mathbb{C}_{ijkl}} = \frac{1}{\left(\boldsymbol{S} \cdot \mathbb{C}^{-1}[\boldsymbol{S}]\right)^2}\left(\boldsymbol{S} \cdot \left(\mathbb{C}^{-1}\frac{\mathrm{D}\mathbb{C}}{\mathrm{D}\mathbb{C}_{ijkl}}\mathbb{C}^{-1}\right)[\boldsymbol{S}]\right). \tag{46}$$

Using the above, we define the shear modulus constraint

$$\gamma \geq \mu_\gamma \bar{\gamma}, \tag{47}$$

where μ_γ is a user-specified parameter and $\bar{\gamma}$ is computed by prescribing $\phi = 1$ throughout the domain, or equivalently computed for an isotropic solid constituent material as $\bar{\gamma} = \frac{E}{2(1+\nu)}$.

2.4.3 Anisotropy

We also require our periodic structures to exhibit some degree of isotropy. A number of anisotropy indices have been presented in the literature, including the universal elastic anisotropy index (Ranganathan and Ostoja-Starzewski 2008) defined by

$$A^{\mathrm{U}} = \frac{\kappa^{\mathrm{V}}}{\kappa^{\mathrm{R}}} + 5\frac{\gamma^{\mathrm{V}}}{\gamma^{\mathrm{R}}} - 6, \tag{48}$$

where the superscripts V and R denote Voigt and Reuss estimates, respectively. These estimates are computed directly from the components of $\mathbb{C}$ (Hill 1952), and so the sensitivity analysis of A^{U} is a simple matter of arithmetic that is omitted here. The universal elastic anisotropy index is motivated from the fact that the Voigt and Reuss estimates of bulk and shear moduli are equal when a material is isotropic, thus by measuring the ratio between these estimates it is possible to quantify how close a material is to isotropic. The universal elastic anisotropy index was later extended to compute the distance between the Voigt and Reuss estimates in log-Euclidean space (Kube 2016) as

$$A^{\mathrm{L}} = \sqrt{\log^2\left(\frac{\kappa^{\mathrm{V}}}{\kappa^{\mathrm{R}}}\right) + 5\log^2\left(\frac{\gamma^{\mathrm{V}}}{\gamma^{\mathrm{R}}}\right)} \tag{49}$$

as an attempt to physically describe the level of anisotropy. We again omit its trivial sensitivity analysis. Similarly, the distance between a stiffness tensor $\mathbb{C}$ and the closest isotropic tensor (Moakher and Norris 2006) can be computed by

$$A^{\mathrm{D}} = ||\log\left(\mathbb{C}^{\mathrm{iso}}\right) - \log(\mathbb{C})||, \tag{50}$$

where $\mathbb{C}^{\mathrm{iso}}$ is the closest isotropic stiffness tensor to $\mathbb{C}$ in log-Euclidean space. It was proven that

$$\log\left(\mathbb{C}^{\mathrm{iso}}\right) = \mathbb{P}^{\mathrm{iso}}\log(\mathbb{C}), \tag{51}$$

where the projection $\mathbb{P}^{\mathrm{iso}}$ is defined in Moakher and Norris (2006) and hence we can compute the anisotropy measure as

$$A^{\mathrm{D}} = ||\mathbb{P}^{\mathrm{iso}}\log(\mathbb{C}) - \log(\mathbb{C})||. \tag{52}$$

To use A^{D} in a constraint we must compute its sensitivity with respect to $\mathbb{C}$. We define $\mathbb{D} = \mathbb{P}^{\mathrm{iso}}\log(\mathbb{C}) - \log(\mathbb{C})$ and derive the sensitivity as

$$\begin{aligned}\frac{\mathrm{D}A_{\log}}{\mathrm{D}\mathbb{C}} \cdot \mathbb{U} &= \frac{1}{2||\mathbb{D}||}\left(\frac{\mathrm{D}}{\mathrm{D}\mathbb{C}}(\mathbb{D} \cdot \mathbb{D})\right) \cdot \mathbb{U} \\ &= \frac{1}{2||\mathbb{D}||}2\mathbb{D} \cdot \frac{\mathrm{D}\mathbb{D}}{\mathrm{D}\mathbb{C}}[\mathbb{U}] \\ &= \frac{1}{||\mathbb{D}||}\left(\left(\frac{\mathrm{D}\mathbb{D}}{\mathrm{D}\mathbb{C}}\right)^T[\mathbb{D}]\right) \cdot \mathbb{U}\end{aligned} \tag{53}$$

for an arbitrary 4*th*-order tensor $\mathbb{U}$. Using the arbitrariness of $\mathbb{U}$, we obtain

$$\frac{\mathrm{D}A_{\log}}{\mathrm{D}\mathbb{C}} = \frac{1}{||\mathbb{D}||}\left(\frac{\mathrm{D}\mathbb{D}}{\mathrm{D}\mathbb{C}}\right)^T[\mathbb{D}]. \tag{54}$$

Note that we obtain the simplification using the projection properties

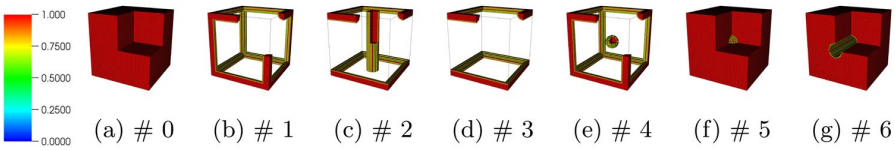

Fig. 5 Exemplary unit cells for constraint evaluation comparison

Table 1 Constraint function values

Unit cell	θ_{vtv}	θ_{vts}	θ_{eig}	θ_{swc}	κ	γ	A^U	A^L	A^D
# 0	0.0e+00	3.1e−01	1.4e+01	9.2e−01	8.3e−01	3.9e−01	7.8e−16	5.1e−16	9.6e−16
# 1	3.2e−01	5.5e−01	1.4e+00	4.9e−01	1.3e−02	7.1e−04	2.5e+01	4.0e+00	3.4e+00
# 2	3.2e−01	6.9e−01	8.1e−07	1.3e+05	1.1e−02	7.4e−09	2.7e+06	3.0e+01	1.6e+01
# 3	3.2e−01	5.9e−01	1.1e+00	7.3e+04	1.5e−08	6.8e−09	2.9e+06	3.2e+01	1.7e+01
# 4	3.2e−01	3.2e+05	2.2e−06	5.7e+03	1.3e−02	7.1e−04	2.5e+01	4.0e+00	3.4e+00
# 5	3.4e+05	3.1e−01	1.4e+01	9.2e−01	8.2e−01	3.8e−01	2.0e−08	8.8e−09	1.4e−04
# 6	6.9e−01	3.1e−01	1.2e+01	9.2e−01	7.6e−01	3.6e−01	2.6e−03	1.1e−03	5.0e−02

$$\left(\frac{\mathrm{D}\mathbb{D}}{\mathrm{D}\mathbb{C}}\right)^T[\mathbb{D}] = \left(\mathbb{P}^{\text{iso}}\frac{\mathrm{D}\log(\mathbb{C})}{\mathrm{D}\mathbb{C}} - \frac{\mathrm{D}\log(\mathbb{C})}{\mathrm{D}\mathbb{C}}\right)^T[\mathbb{D}] = -\left(\frac{\mathrm{D}\log(\mathbb{C})}{\mathrm{D}\mathbb{C}}\right)^T[\mathbb{D}] \tag{55}$$

since

$$\left(\mathbb{P}^{\text{iso}}\right)^T[\mathbb{D}] = \left(\mathbb{P}^{\text{iso}}\right)^T\left[\mathbb{P}^{\text{iso}}\log(\mathbb{C}) - \log(\mathbb{C})\right] = \mathbb{P}^{\text{iso}}\log(\mathbb{C}) - \mathbb{P}^{\text{iso}}\log(\mathbb{C}) = \mathbf{0}. \tag{56}$$

Finally, we obtain

$$\frac{\mathrm{D}A_{\log}}{\mathrm{D}\mathbb{C}} = \frac{-1}{||\mathbb{D}||}\left(\frac{\mathrm{D}\log(\mathbb{C})}{\mathrm{D}\mathbb{C}}\right)^T[\mathbb{D}]. \tag{57}$$

3 Constraint efficacy comparison

A series of exemplary unit cell designs are presented in Fig. 5 to highlight the capabilities and limitations of the proposed optimization constraints. Each image displays the solid phase volume fractions of the example unit cell, using the threshold $\phi = 0.5$ for visualization purposes. Additionally, an octant has been clipped from each unit cell to illustrate internal features. Table 1 denotes each scalar metric defined in Sect. 2 evaluated on a mesh of 60^3 uniform hexahedral elements. The isotropic base material has a Young's modulus of $E = 1$ and a Poisson's ratio of $\nu = 0.3$. The ersatz void material uses $\varepsilon = 10^{-8}$. All PDE's were solved using the open-source, modular finite element method (MFEM) (Anderson et al. 2021) library developed by Lawrence Livermore National Laboratory.

We begin the discussion by considering the uniform, solid microstructure ($\phi = 1$), referred to as unit cell #0. The evaluations of θ_{vt}, θ_{eig}, and θ_{swc} serve as our baseline values, i.e., $\bar{\theta}_{\text{vt}}$, $\bar{\theta}_{\text{eig}}$, and $\bar{\theta}_{\text{swc}}$, respectively. The homogenized κ and γ are verified by comparing them to the analytical expressions $\kappa = \frac{E}{3(1-2\nu)}$ and $\gamma = \frac{E}{2(1+\nu)}$. Finally, we notice that all 3 anisotropy measures are 0 (within numerical precision), which is expected since our unit cell material is isotropic.

Next, we consider a microstructure consisting of orthogonal beams aligned with the Cartesian axes, denoted as unit cell #1. This unit cell is presented as an example of an acceptable design; it is self-supporting, exhibits reasonable stiffness in all directions, and does not have EVS or ISM. Moving left to right across Table 1 we see that $\theta_{\text{vtv}} = 1.03\,\bar{\theta}_{\text{vt}}$, while $\theta_{\text{vts}} = 1.77\bar{\theta}_{\text{vt}}$. Both of these values would be acceptable if μ_{vt} was selected in the range of 4–10 as recommended (Liu et al. 2015). Thus, the VTM constraints would correctly indicate that neither ISM nor EVS exist in the microstructure. We notice that $\theta_{\text{eig}} \approx 10^{-1}\bar{\theta}_{\text{eig}}$ and as expected we see a smaller self-weight compliance than our baseline structure. The homogenized κ and γ are, again as expected, also lower than the baseline microstructure, but nonetheless we have non-zero bulk and shear stiffness. The anisotropy measures all predict a moderate amount of anisotropy, which is also expected for this orthotropic unit cell. In summary, all of the constraints behave as we desire.

If we consider the effect of moving the vertical rods from unit cell #1 so they do not intersect with the horizontal sets of rods, we arrive at unit cell #2. Table 1 reveals that $\theta_{\text{vtv}} = 1.03\,\bar{\theta}_{\text{vt}}$, correctly communicating a lack of EVS. It would be fair at this point to suspect that θ_{vts} could rise dramatically since the vertical rods are not in contact with the horizontal rods. However, we see that $\theta_{\text{vts}} = 2.23\,\bar{\theta}_{\text{vt}}$. This can be understood by recognizing that the rods are infinitely

long, under the infinite periodicity assumption. Thus, we have our first constraint limitation; the VTM identifies only those ISM enclosed by the unit cell, i.e., it does not ensure self-supporting structures. Fortunately, we have constraints that can identify these circumstances. Namely, the two functions $\theta_{\text{eig}} \approx 10^{-7}\bar{\theta}_{\text{eig}}$ and $\theta_{\text{swc}} \approx 10^{5}\bar{\theta}_{\text{swc}}$ both identify that unit cell # 2 is not self-supporting. Interestingly, we see that κ from unit cell #2 is similar to that of unit cell #1 demonstrating that disconnected rods do not adversely affect the ability to support a pressure load. However, $\gamma \approx 10^{-8}\bar{\gamma}$ demonstrating almost no resistance to a shear load. As expected, all anisotropy indices show stark increases, but A^L and A^D show much smaller increases than A^U due to their dependencies on the logarithm.

Unit cell #3 is similar to #1 and #2; however, the vertical rods have been removed. This example was contrived to illustrate a potential pitfall of θ_{eig}. We notice that $\theta_{\text{eig}} \approx 10^{-1}\bar{\theta}_{\text{eig}}$ even though it is clear that the structure is disconnected. This behavior is due to the fact that all of the solid phase material in the unit cell is connected, thus we have only 3 zero-valued eigenvalues. This non self-supporting structure is identified, however, by noting that $\theta_{\text{swc}} \approx 10^{5}\bar{\theta}_{\text{swc}}$. Alternatively, it is identified by noting that $\kappa \approx 0$ and $\gamma \approx 0$, while the isotropy indices increase significantly. As seen here, a constraint on bulk stiffness, shear stiffness, or anisotropy could be used in conjunction with θ_{eig} to ensure a self-supporting structure.

The strengths of our ISM constraints are demonstrated with unit cell #4. The small sphere of floating material is easily identified as $\theta_{\text{vts}} \approx 10^{6}\bar{\theta}_{\text{vt}}$, $\theta_{\text{eig}} \approx 10^{-7}\bar{\theta}_{\text{eig}}$, and $\theta_{\text{swc}} \approx 10^{3}\bar{\theta}_{\text{swc}}$. Each of these metrics provides a clear signal that an ISM exists. As expected, κ, μ, and all of the anisotropy indices return the same values as their corresponding evaluations on unit cell #1, since the floating sphere has no effect on the homogenized constitutive tensor.

Finally, the effectiveness of θ_{vtv} is demonstrated with unit cells #5 and #6. The void space in unit cell #6 is acceptable since support material or pre-sintered powder could be removed, whereas the void space in unit cell #5 is unacceptable. The VTM is able to distinguish these cases as $\theta_{\text{vtv}} \approx 10^{6}\bar{\theta}_{\text{vt}}$ for unit cell #5 whereas $\theta_{\text{vtv}} = 2.23\bar{\theta}_{\text{vt}}$ for unit cell #6.

The results presented in Table 1 elucidate the capabilities and limitations of our constraints for producing manufacturable designs. For example, if the manufacturing process cannot handle EVS, then a θ_{vtv} constraint should be enforced. The simplest technique to ensure self-supporting structures is to enforce the θ_{swc} constraint. The downside, however, is that the stiffness cannot be explicitly tuned via θ_{swc}. If the designer seeks to tune the level of bulk or shear stiffness, then κ or γ constraints, respectively, are required. In many cases, these stiffness constraints are sufficient to remove unsupported material since ISM do not add stiffness to the structure; however, ISM are not explicitly forbidden. Because of this the κ or γ constraints should be augmented with either a θ_{vts}, θ_{eig}, or θ_{swc} constraint. Finally, if isotropy is required for a particular application, then any of the proposed anisotropy constraints should be enforced.

The choice of which combination of constraints to enforce may also be dictated by computational expense. The VTM and self-weight compliance problems require an array of 2^d unit cells, although the VTM partial differential equation (PDE) is a scalar problem whereas the self-weight compliance PDE is a vector problem. If the unit cell exhibits orthorhombic symmetry, the self-weight compliance computations can be performed over a single unit cell whereas the VTM always requires an array of 2^d unit cells. The mechanical eigenvalue problem in general requires a single unit cell domain, but the mesh can be reduced to an octant for cells with orthorhombic symmetry (Barbarosie et al. 2017). Also, κ, γ, and the anisotropy measures are derived from the same homogenized stiffness tensor, thus only one homogenization computation is required over a single unit cell, or over an octant when unit cells exhibit orthorhombic symmetry (Barbarosie et al. 2017). To conclude, a designer should select a combination of constraints that ensures their designs are viable with respect to manufacturing, stiffness, and anisotropy requirements. Then, the computational cost should be considered based on the symmetry of the unit cell. The computational cost of the constraints may be somewhat mitigated if the PDE solutions, e.g., the eigenvalues or the homogenized stiffness tensor, are required for other aspects of the TO framework since the scalar quantities are much cheaper to compute than the PDE solutions.

4 Optimization test problem

We now demonstrate the effectiveness of the proposed constraints and point out their capabilities and limitations on a simple topology optimization problem. Consider a cubic unit cell of side length a centered at the origin with imposed orthorhombic symmetry, uniformly discretized by 60^3 voxels. The 30^3 voxel volume fractions in the octant symmetry cell serve as the design parameters. The length scale is controlled by applying a symmetric, periodic cone filter with a filter radius of $0.05a$, cf. (Swartz et al. 2021). In all cases, the initial design is uniform with $\phi = 0.5$. A SIMP exponent of $q = 3$ and a modified SIMP exponent of $r = 6$ are used for the VTM, eigenvalue, and self-weight compliance constraints. A SIMP exponent of $q = 4$ is used for the homogenized-based constraints, i.e., bulk modulus, shear modulus, and isotropy constraints. The modified SIMP volume fraction boundaries are $\phi_{\text{L}} = 0.2$ and $\phi_{\text{U}} = 0.8$, and the ersatz void phase uses $\varepsilon = 10^{-8}$. All optimization problems

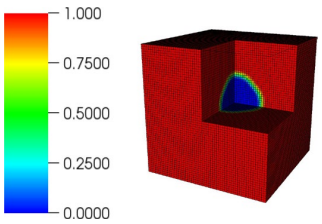

Fig. 6 Optimal ϕ solutions for θ_{EVS}

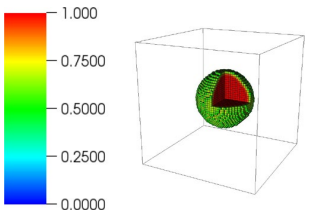

Fig. 8 Optimal ϕ solutions for θ_{ISM}

Fig. 7 Optimal ϕ solutions for θ_{EVS} with θ_{vtv} constraint

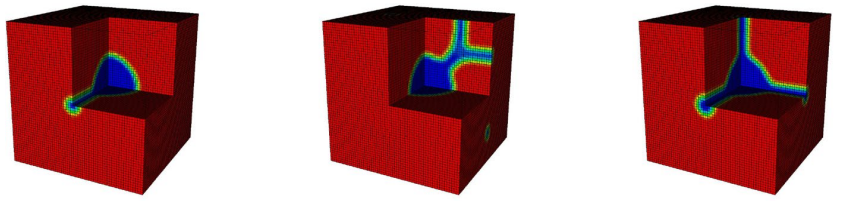

(a) $\mu_{\text{vtv}} = 25.0$ (b) $\mu_{\text{vtv}} = 12.0$ (c) $\mu_{\text{vtv}} = 6.0$

were solved with the open-source, interior point optimizer (IPOPT) (Wächter and Biegler 2006).

4.1 Virtual temperature method for EVS identification

Consider the optimization problem

$$\min_{\boldsymbol{\phi}} \quad \theta_{\text{EVS}} = \sum_{i=1}^{N_{\text{voxel}}} \begin{cases} 1-\phi_i & r_i \geq r_0 \\ \phi_i & r_i < r_0 \end{cases} \tag{58}$$

$$\text{subject to} \quad 0 \leq \phi_i \leq 1,$$

where r_i is the distance from the voxel i centroid to the origin. The solution is a solid unit cell with a hollow sphere removed from the center, cf. Fig. 6. The resulting structure is problematic due to the region of EVS. To address this issue, we again solve Eq. (58) with the Eq. (7) constraint using the material interpolations from Eqs. (2) and (3). A series of optimal designs for various values of μ_{vtv} are presented in Fig. 7. We see that for $\mu_{\text{vtv}} = 25.0$, a channel of void space is formed effectively eliminating the EVS. For $\mu_{\text{vtv}} = 12.0$, a channel with two forks appears, and finally for $\mu_{\text{vtv}} = 6.0$, channels are created in all 3 dimensions. Thus, any of the selected values of μ_{vtv} eliminate the EVS. A trade-off exists between "how enclosed" the sphere is and the optimal value of the objective function, thus proper selection of μ_{vtv} will certainly be problem specific.

4.2 Virtual temperature method for ISM identification

Now we consider the optimization problem

$$\min_{\boldsymbol{\phi}} \quad \theta_{\text{ISM}} = \sum_{i=1}^{N_{\text{voxel}}} \begin{cases} 1-\phi_i & r_i \leq r_0 \\ \phi_i & r_i > r_0 \end{cases} \tag{59}$$

$$\text{subject to} \quad 0 \leq \phi_i \leq 1.$$

The result is a unit cell consisting of a floating sphere at the origin, cf. Fig. 8.[1] The resulting structure is problematic due to the ISM. To address this issue we again solve Eq. (59) with the Eq. (7) constraint using the material interpolations from Eqs. (8) and (9). A series of optimal designs for various values of μ_{vts} are presented in Fig. 9. We see very similar results to those in Sect. 4.1. For $\mu_{\text{vts}} = 25.0$, a beam of solid material is formed effectively eliminating the ISM. For $\mu_{\text{vts}} = 12.0$, a beam with two forks appears, and finally for $\mu_{\text{vts}} = 6.0$, beams are created in all 3 dimensions. Thus, any of the selected values of μ_{vts} eliminate ISM and adjusting the value of μ_{vts} is the choice of the designer. A notable downside to this constraint is that we cannot guarantee the periodic structure is self-supporting, as evidenced by the $\mu_{\text{vts}} = 25.0$ and 12.0 designs, which do not have stiffness in all directions.

[1] In Sects. 4.2–4.5 only volume fractions satisfying $\phi > 0.5$ are plotted for visualization.

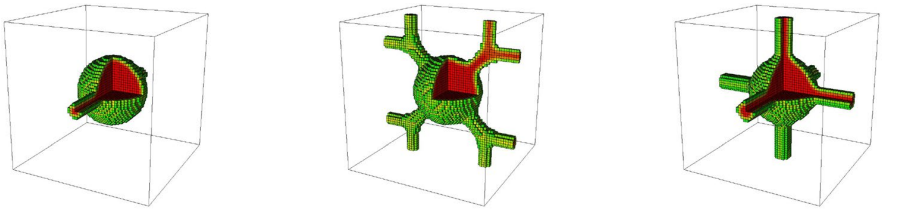

(a) $\mu_{\text{vts}} = 25.0$ (b) $\mu_{\text{vts}} = 12.0$ (c) $\mu_{\text{vts}} = 6.0$

Fig. 9 Optimalϕ solutions for θ_{ISM} with θ_{vts} constraint

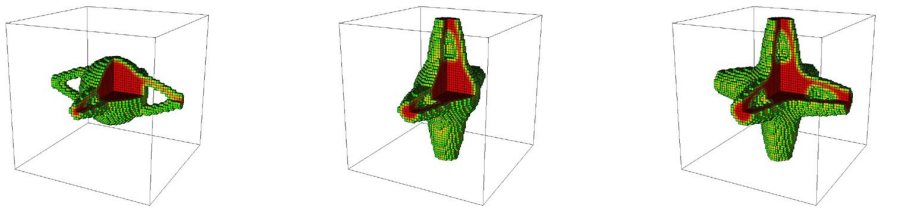

(a) $\mu_{\text{eig}} = 0.03$ (b) $\mu_{\text{eig}} = 0.10$ (c) $\mu_{\text{eig}} = 0.15$

Fig. 10 Optimal ϕ solutions for θ_{ISM} with θ_{eig} constraint

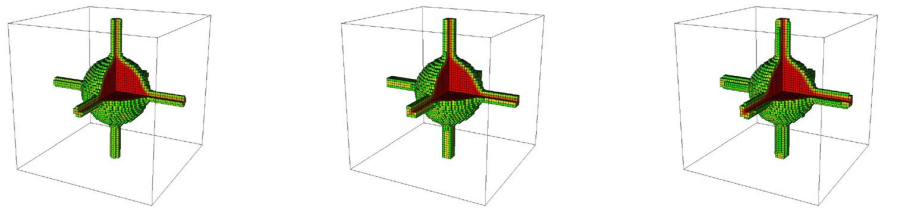

(a) $\mu_{\text{swc}} = 2.0$ (b) $\mu_{\text{swc}} = 1.5$ (c) $\mu_{\text{swc}} = 1.1$

Fig. 11 Optimal ϕ solutions for θ_{ISM} with θ_{swc} constraint

4.3 Eigenvalue constraint for ISM identification

To demonstrate the eigenvalue constraint we solve the optimization problem in Eq. (59) subject to the Eq. (27) constraint. Optimal structures are presented in Fig. 10 for various values of μ_{eig}. For $\mu_{\text{eig}} = 0.03$, the ISM is effectively removed by adding thin rod-like features, which become slightly larger for $\mu_{\text{eig}} = 0.10$. However, neither of these designs are self-supporting. If we use $\mu_{\text{eig}} = 0.15$, we remove the ISM and obtain a self-supporting structure. In summary, we observe similar behavior between the mechanical eigenvalue constraint and the ISM constraint in Sect. 4.2. For certain values of μ_{eig} we can remove the ISM without generating self-supporting structures. The appropriate value of μ_{eig} is again problem dependent. We also note that the optimal designs for $\mu_{\text{eig}} = 0.10$ and 0.15 exhibit EVS. In fact, none of our ISM constraints prohibit EVS, which motivates our use of both ISM and EVS constraints to produce manufacturable designs in Sect. 5.4.

4.4 Self-weight compliance constraint for ISM identification

We demonstrate the self-weight compliance constraint by solving the optimization problem in Eq. (59) subject to the Eq. (35) constraint. Optimal structures are presented in Fig. 11 for various values of μ_{swc}. We immediately notice that this constraint yields similar results for the three presented values of μ_{swc}. A slight difference appears in the thickness of the supporting beams, but the topology is identical in all cases. Most importantly, all three designs are fully

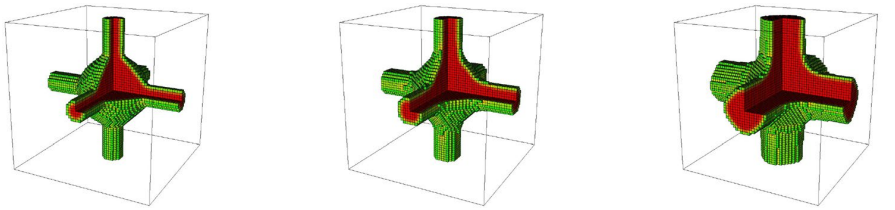

(a) $\mu_\kappa = 0.005$ (b) $\mu_\kappa = 0.01$ (c) $\mu_\kappa = 0.03$

Fig. 12 Optimal ϕ solutions for θ_{ISM} with θ_κ constraint

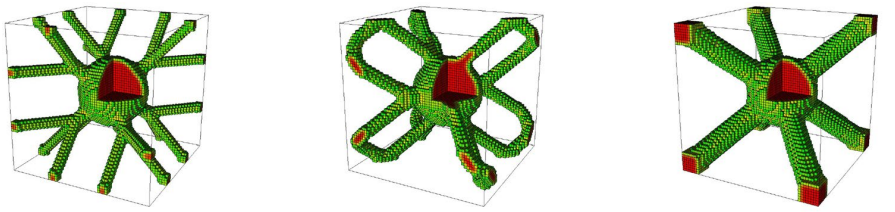

(a) $\mu_\gamma = 0.005$ (b) $\mu_\gamma = 0.01$ (c) $\mu_\gamma = 0.03$

Fig. 13 Optimal ϕ solutions for θ_{ISM} with θ_γ constraint

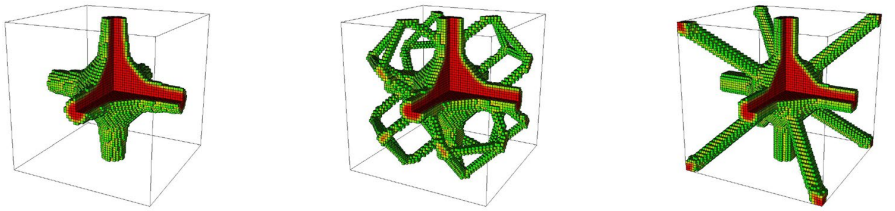

(a) $A^U < 15.0$ (b) $A^U < 5.0$ (c) $A^U < 1.0$

Fig. 14 Optimal ϕ solutions for θ_{ISM} with θ_κ (μ_κ=0.01) and A^U constraints

self-supporting. Thus, we expect that the appropriate μ_{swc} value is less problem dependent. The downsides of this constraint are its computational expense and its inability to tune stiffness. The latter concern is addressed in the next section.

4.5 Effective property constraints

If a design requires a particular level of stiffness or isotropy, effective property constraints derived from a homogenization analysis may be employed. We investigate a few possibilities here. First, we solve the Eq. (59) optimization problem subject to the Eq. (43) constraint. Optimal structures for various values of μ_κ are presented in Fig. 12. As expected, the features become larger as μ_κ is increased, and in all cases we have stiffness in all directions. The optimal structures are fairly intuitive considering the bulk modulus measures the resistance to pressure loads.

Similarly, we solved the Eq. (59) optimization problem subject to the Eq. (47) constraint. Again, the features become larger as μ_γ is increased, and in all cases we have stiffness in all directions. The structures in Fig. 13 exhibit more geometric complexity than the structures in Fig. 12, which is apparently advantageous for resisting deflection under shear loads.

We have guaranteed through our definitions of κ and γ that enforcement of Eqs. (43) or (47) constraints yields structures with stiffness in all directions. However, no consideration is made with respect to isotropy. If isotropy is desired we, e.g., augment the bulk modulus constraint with a constraint on A^U, A^L, or A^D, cf. Figs. 14, 15, and 16. We obtain very similar structures when constraining A^U and A^L, which is not surprising since they are both derived from Voigt and Reuss stiffness estimates. It is expected that these three constraints yield similar results since they are measuring the same type of behavior. Thus, we do not give preference to any of the anisotropy measures, although ease of implementation may favor the use of A^U or A^L over A^D.

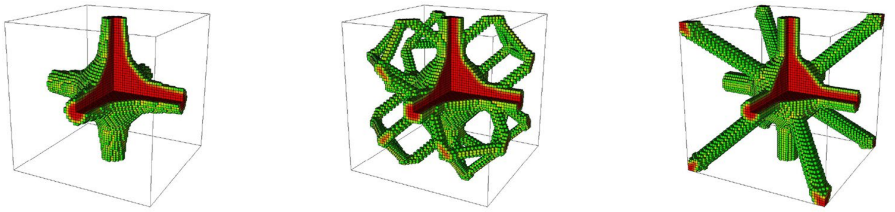

(a) $A^L < 3.0$ (b) $A^L < 1.0$ (c) $A^L < 0.1$

Fig. 15 Optimal ϕ solutions for θ_{ISM} with θ_κ (μ_κ=0.01) and A^L constraints

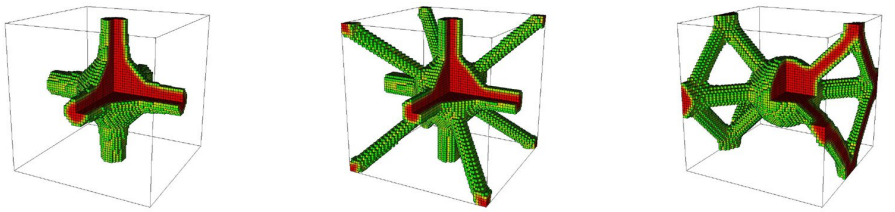

(a) $A^D < 3.0$ (b) $A^D < 1.0$ (c) $A^D < 0.1$

Fig. 16 Optimal ϕ solutions for θ_{ISM} with θ_κ (μ_κ=0.01) and A^D constraints

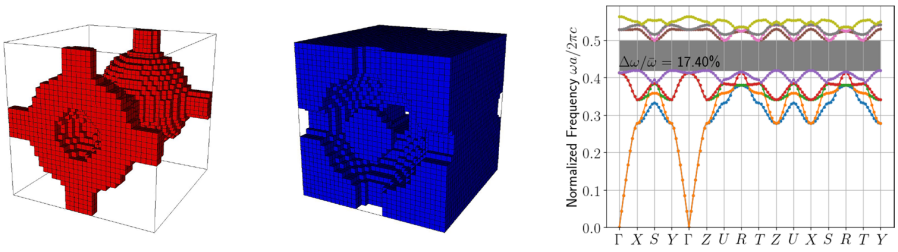

(a) Unconstrained

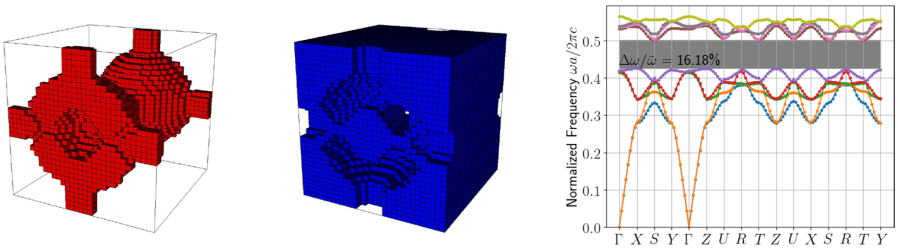

(b) Constrained with $\mu_{\text{vtv}} = 6.0$

Fig. 17 Applying θ_{vtv} constraint to remove EVS from mode 5-6 bandgap structure

5 Photonic crystal design with manufacturing constraints

The constraints formulated in Sect. 2 are used to design photonic crystals for complete bandgaps. A topology optimization framework for photonic crystal design was recently presented (Swartz et al. 2021), which allows the bandgap optimizations to be performed using a traditional gradient-based NLP solver. This capability is augmented here by imposing design constraints to resolve deficiencies in our previous photonic crystal designs that were not manufacturable or self-supporting (Swartz et al. 2021). Note that throughout Sect. 5 the volume fractions have been thresholded such that $\phi \geq 0.5$ is considered solid material, whereas $\phi < 0.5$ is considered void space in the dispersion analyses. Please see the original manuscript (Swartz et al. 2021) for

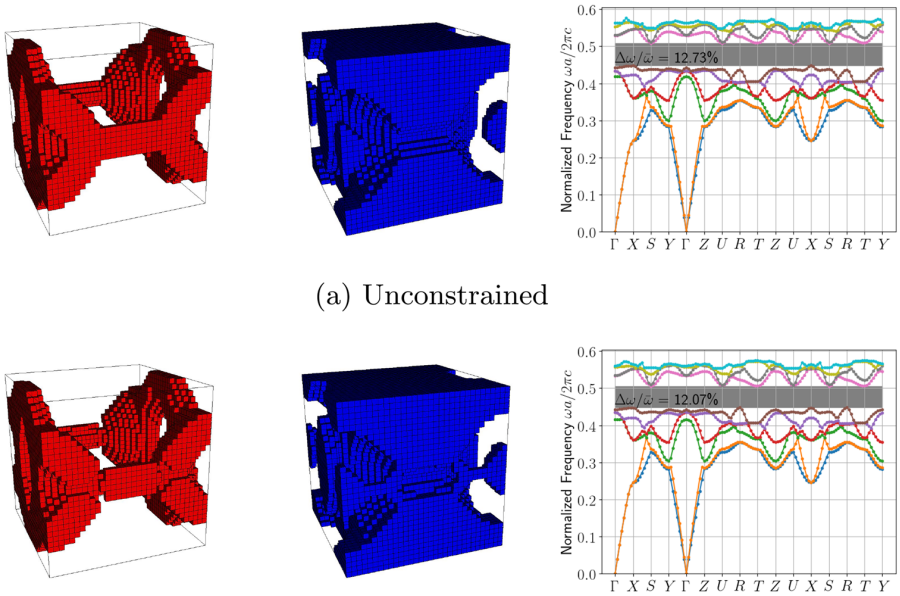

Fig. 18 Applying θ_{vtv} constraint to remove EVS from mode 6–7 bandgap structure

a comprehensive description of the problem formulation, photonic bandgap definition, and other relevant details.

5.1 Removal of EVS

Two recently published designs (Swartz et al. 2021) for photonic crystals with complete 3D bandgaps displayed EVS, which we now remove via the VTM constraint. Figure 17a displays the published optimal bandgap structure (Swartz et al. 2021); the left-most image displays the solid material, while the middle image displays the complement, i.e., the void space. We immediately notice a disconnected void space region causing EVS. The dispersion plot reveals a 17.40% bandgap–midgap ratio. We solve the optimization problem enforcing the Eq. (7) constraint with $\mu_{\text{vtv}} = 6.0$ to obtain the design depicted in Fig. 17b. The constrained design is similar to the unconstrained design; however, small channels have formed causing the void space to be simply connected. Thus, support material or pre-sintered powder could be removed from the design (Liu et al. 2015). There is a slight reduction in the bandgap–midgap ratio, i.e., 16.18% vs. 17.40%, but this difference is small considering that the previous design was not manufacturable.

Another problematic 3D bandgap design from Swartz et al. (2021) is pictured in Fig. 18. The design exhibited a bandgap–midgap ratio of 12.73%; however, a region of EVS is present. Enforcing the Eq. (7) constraint with $\mu_{\text{vtv}} = 4.0$ produces the design depicted in Fig. 18b. Again, we see the formation of small channels causing the void space to be simply connected. The bandgap–midgap ratio of this design is reduced to 12.07%, but we again have produced a manufacturable structure.

5.2 Removal of ISM

The bandgap structure depicted in Fig. 19a from Swartz et al. (2021), exhibits ISM. The optimization problem is resolved with a variety of constraints to prevent ISM. First, the VTM Eq. (7) constraint is enforced. The resulting structure depicted in Fig. 19b has a slightly smaller bandgap; however, something interesting has occurred. The topology of the structure has changed such that both the ISM and EVS present in the original design are removed. Interestingly, the designs illustrated in Figs. 19c and 19d, obtained via enforcement of the self-weight compliance and shear modulus constraints, respectively, outperform the unconstrained design. It appears that the constrained optimizations found a better local minima than the unconstrained. This behavior should not be expected in general, but it is an important finding nonetheless. The downside to the designs pictured in Figs. 19c and d is that EVS remains, which is not surprising since EVS is not strictly forbidden in the optimization formulations. This point is further addressed in Sect. 5.4.

5.3 Requirement of self-supporting structure

A recently published structure with a complete 2D bandgap (Swartz et al. 2021) is not self-supporting. Specifically, the design, pictured in Fig. 20a, is not self-supporting as it consists of two separate solid regions. To alleviate this issue we first re-solved the problem while enforcing the Eq. (27) mechanical eigenvalue constraint. The optimized design shown in Fig. 20b is similar to the unconstrained version,

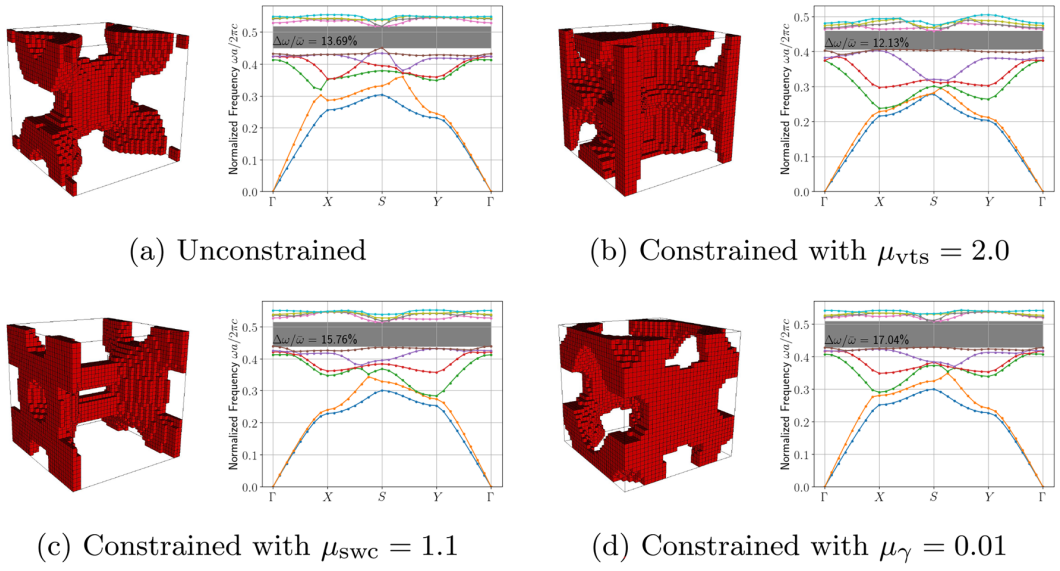

(a) Unconstrained (b) Constrained with $\mu_{\text{vts}} = 2.0$

(c) Constrained with $\mu_{\text{swc}} = 1.1$ (d) Constrained with $\mu_{\gamma} = 0.01$

Fig. 19 Applying various constraints to remove ISM

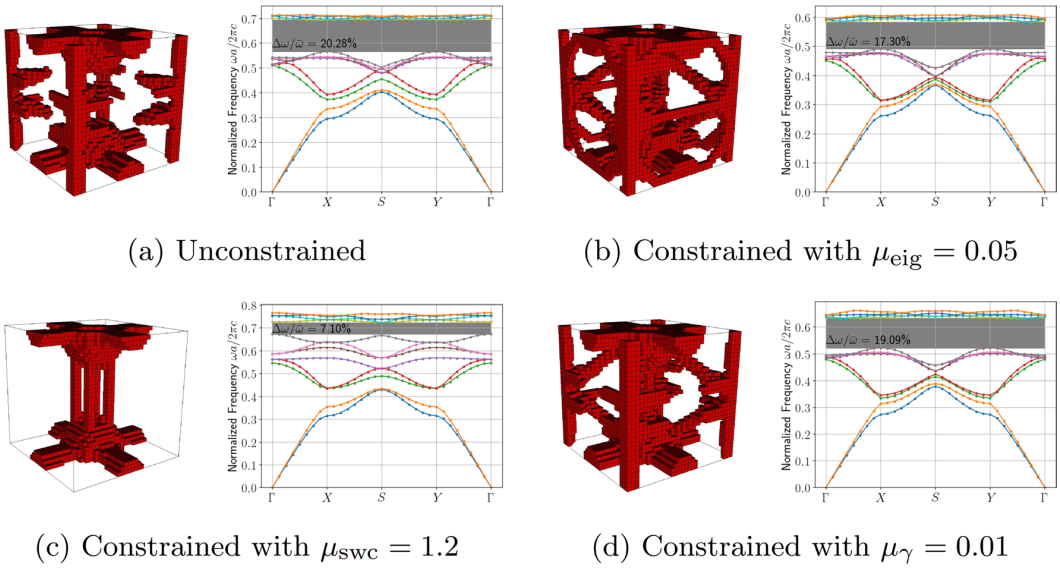

(a) Unconstrained (b) Constrained with $\mu_{\text{eig}} = 0.05$

(c) Constrained with $\mu_{\text{swc}} = 1.2$ (d) Constrained with $\mu_{\gamma} = 0.01$

Fig. 20 Applying various constraints to ensure structures are self-supporting

but additional features have been added so that the structure is fully self-supporting. The bandgap performance deceases slightly, but the design is now manufacturable. We next enforced the Eq. (35) self-weight compliance constraint. The optimal structure seen in Fig. 20c is quite different from the unconstrained design, and the bandgap performance is significantly reduced. All is not lost, however, as the structure is fully self-supporting and still exhibits a complete bandgap. Finally, we enforced the Eq. (47) shear modulus constraint. The resulting optimal structure appearing in Fig. 20d is similar to the Fig. 20b design in that additional features have been added; however, the performance is better. We want to emphasize that these results are just examples proving the effectiveness of the constraints and that more exhaustive studies may lead to different conclusions about which of the presented constraints produce better performing designs.

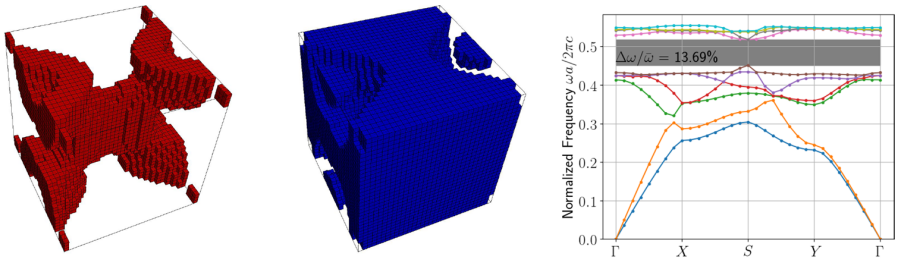

(a) Unconstrained

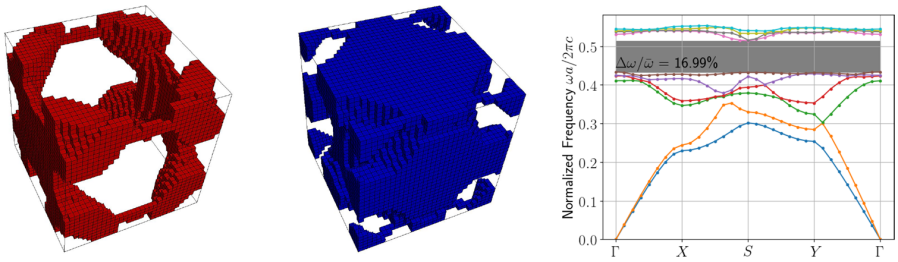

(b) Constrained with $\mu_\kappa = 0.01$ and $\mu_{\text{vtv}} = 4.0$

Fig. 21 Applying κ and VTM constraints to ensure structures are manufacturable

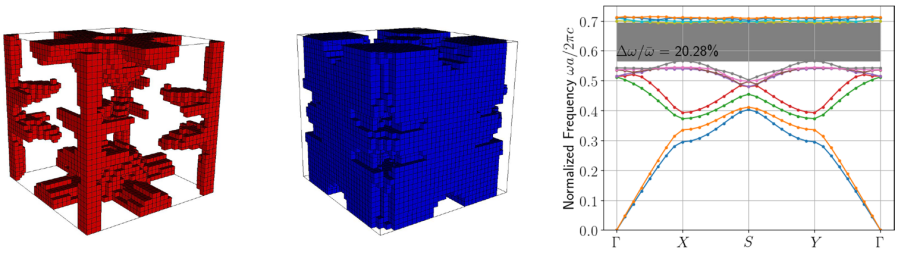

(a) Unconstrained

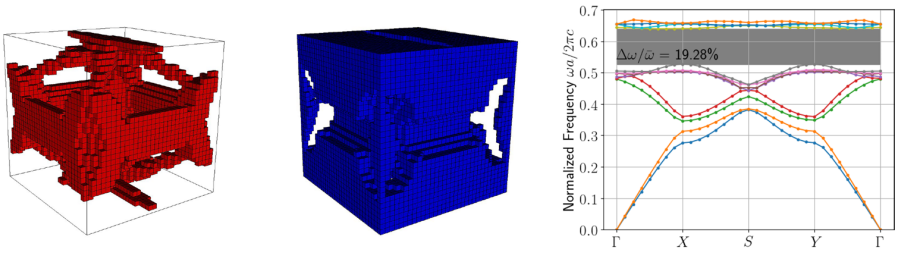

(b) Constrained with $\mu_\gamma = 0.01$ and $\mu_{\text{vtv}} = 8.0$

Fig. 22 Applying γ and VTM constraints to ensure structures are manufacturable

5.4 Manufacturable photonic crystals

In order to manufacture our photonic crystals they must neither exhibit EVS nor ISM, i.e., it is not enough to consider them separately. To this end, we reconsidered the design problems addressed in Sects. 5.2 and 5.3. We began by optimizing the 2D bandgap–midgap ratio between modes 6 and 7 with a bulk modulus constraint to ensure stiffness and a VTM constraint to remove EVS. The resulting constrained structure is compared to the original unconstrained structure in Fig. 21. Notice that both the ISM and EVS have been removed from the design, while simultaneously improving the bandgap performance.

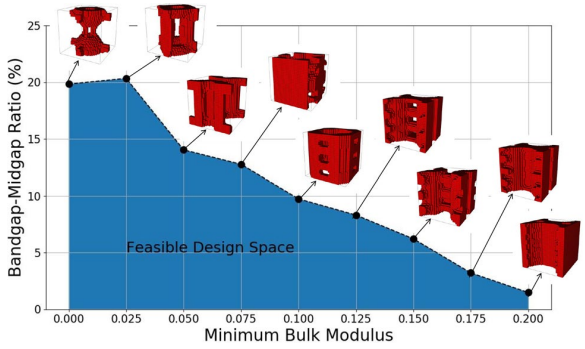

Fig. 23 2D Bandgap–midgap ratio θ_ω vs. bulk modulus κ

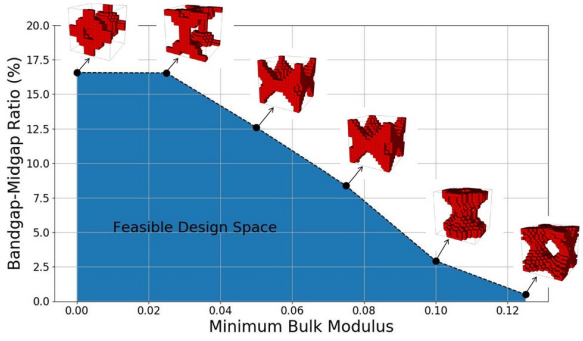

Fig. 24 3D Bandgap–midgap ratio θ_ω vs. bulk modulus κ

Similarly, we optimized the 2D bandgap–midgap ratio between modes 8 and 9 with a shear modulus constraint to ensure stiffness and a VTM constraint to remove EVS. The resulting design, pictured in Fig. 22, is quite different from its unconstrained counterpart illustrated in Fig. 22a. Both ISM and EVS have been eliminated in the constrained design which is also self-supporting. Again we emphasize that although the bandgap–midgap ratio is reduced from 20.28 to 19.28%, the new design is manufacturable.

6 Photonic bandgap design with tunable bulk modulus

If a designer seeks a photonic crystal with a desired stiffness, the bulk modulus and shear modulus constraints should be considered. To demonstrate this capability, a series of bandgap optimizations are performed with various minimum bulk modulus constraints. At each constraint value, 20 random initial designs were used from which the best resulting optimized design is selected.

Figure 23 plots the optimal bandgap–midgap ratio for a complete 2D bandgap between modes 5 and 6 against the minimum bulk modulus. The best of the 20 optimized designs is pictured near its corresponding data point; the shaded region under the curve indicates the feasible design space. We see a roughly inverse linear relationship between our two quantities of interest and note that $\kappa \approx 0.2$ is the largest bulk stiffness we can generate with a complete bandgap. This plot allows designers to visualize the trade-off between bandgap and bulk stiffness performance. It is interesting to note that enforcing a minimum bulk modulus of $\kappa \geq 0.025$ actually produced a better performing bandgap structure than optimizing for bandgap without considering κ; evidenced by the non-monotonicity of the plot in Fig. 23. Since there are many local minima in the designs space we cannot hope to capture the global minimum with only 20 initial designs and thus we should interpret the shaded region as an approximation of the feasible design space.

We repeat the Fig. 23 study, but now design for complete 3D bandgaps between modes 5 and 6. The results, pictured in Fig. 24, present a roughly inverse linear relationship between the two quantities of interest and suggest that $\kappa \approx 0.12$ is the largest bulk stiffness we can generate with a complete bandgap. As expected, the volume fraction increases with κ in Fig. 24, but the topology does not change in contrast to the Fig. 23 designs.

7 Conclusions

Topology optimization of phononic/photonic crystals often generates structures that are not manufacturable due to EVS and ISM. Additionally, they often exhibit poor stiffness. We have suggested a series of simple constraints which can be used to enforce fully-connected, manufacturable structures with stiffness.

The virtual temperature method is used to prevent EVS and extended to prevent ISM. Further, we adapted the VTM to periodic structures such that constraint behavior is invariant with respect to unit cell selection. A mechanical eigenvalue constraint has been proposed to ensure fully-connected structures while the proposed self-weight compliance constraint ensures self-supporting structures. We also studied the effect of homogenization-based constraints on the bulk and shear moduli to ensure desired stiffness and remove ISM, although the latter claim is not guaranteed. Finally, the efficacy of three proposed isotropy constraints have been demonstrated.

The performance of each constraints was demonstrated on contrived test cases and on the design of photonic bandgap structures. We generated 3D structures with complete 2D and 3D photonic bandgaps that were self-supporting and had required levels of stiffness. The trade-off between photonic bandgap and bulk modulus was investigated to generate an approximation of the feasible design space.

It is imperative to use the VTM to prevent EVS if the AM process used to manufacture the designs will require support material or powder. We suggest employing a bulk and/or modulus constraint to ensure a desired degree of stiffness. Augmenting a stiffness constrained formulation with a mechanical eigenvalue constraint or the VTM will eliminate ISM. Alternatively, a self-weight compliance constraint is sufficient if a fully-connected structure is the only design requirement beyond the desired objective. The proposed bulk and shear stiffness constraints require at least some stiffness in all directions. Thus, the isotropic constraints may not be necessary unless, of course, some degree of isotropy is specifically required. There was no discernible difference between the three studied isotropy constraints, although the ease of differentiating and implementing the universal or log-universal isotropy constraints give them a slight advantage over the log-distance constraint.

Future studies should implement these constraints to satisfy the requirements of particular manufacturing processes. This will further elucidate appropriate μ values for the constraint functions and further test the design framework. Additionally, these constraints should be applied to prevent ISM in other applications, such as acoustic filters.

Funding This work was performed under the auspices of the U.S. Department of Energy by LLNL under Contract DE-AC52-07NA27344. Funding from the Graduate Research Scholar Program and LDRD number 20-ERD-020 through LLNL is gratefully acknowledged. LLNL-JRNL-827808-DRAFT.

Declarations

Conflict of interest The authors declare that they have no conflicts of interest.

Replication of results The authors believe sufficient information has been provided to reproduce the presented results.

References

Allaire G (2002) Shape optimization by the homogenization method. Springer, New York. https://doi.org/10.1007/978-3-662-05086-6

Allaire G, Dapogny C, Estevez R, Faure A, Michailidis G (2017) Structural optimization under overhang constraints imposed by additive manufacturing technologies. J Comput Phys 351:295–328. https://doi.org/10.1016/j.jcp.2017.09.041

Anderson R, Andrej J, Barker A, Bramwell J, Camier J-S, Cerveny J, Dobrev V, Dudouit Y, Fisher A, Kolev T, Pazner W, Stowell M, Tomov V, Akkerman I, Dahm J, Medina D, Zampini S (2021) Mfem: a modular finite element methods library. Comput Math Appl 81:42–74. https://doi.org/10.1016/j.camwa.2020.06.009

Andreasen CS, Andreassen E, Jensen JS, Sigmund O (2014) On the realization of the bulk modulus bounds for two-phase viscoelastic composites. J Mech Phys Solids 63:228–241. https://doi.org/10.1016/j.jmps.2013.09.007

Andreassen E, Lazarov BS, Sigmund O (2014) Design of manufacturable 3d extremal elastic microstructure. Mech Mater 69(1):1–10. https://doi.org/10.1016/j.mechmat.2013.09.018

Babaee S, Shim J, Weaver JC, Chen ER, Patel N, Bertoldi K (2013) 3d soft metamaterials with negative poisson's ratio. Adv Mater 25(36):5044–5049. https://doi.org/10.1002/adma.201301986

Barbarosie C, Tortorelli DA, Watts S (2017) On domain symmetry and its use in homogenization. Comput Methods Appl Mech Eng 320:1–45. https://doi.org/10.1016/j.cma.2017.01.009

Bendsøe MP (1989) Optimal shape design as a material distribution problem. Struct Optim 1(4):193–202. https://doi.org/10.1007/BF01650949

Bendsøe MP, Kikuchi N (1988) Generating optimal topologies in structural design using a homogenization method. Comput Methods Appl Mech Eng 71(2):197–224. https://doi.org/10.1016/0045-7825(88)90086-2

Bendsøe MP, Sigmund O (2004) Topology optimization: theory, methods, and applications, 2nd edn. Springer, Berlin. https://doi.org/10.1007/978-3-662-05086-6

de Kruijf N, Zhou S, Li Q, Mai Y-W (2007) Topological design of structures and composite materials with multiobjectives. Int J Solids Struct 44(22–23):7092–7109. https://doi.org/10.1016/j.ijsolstr.2007.03.028

Diaz A, Sigmund O (2010) A topology optimization method for design of negative permeability metamaterials. Struct Multidisc Optim 41(2):163–177. https://doi.org/10.1007/s00158-009-0416-y

Ding Y, Liu Z, Qiu C, Shi J (2007) Matameterial with simultaneously negative bulk modulus and mass density. Phys Rev Lett 99(9):093904. https://doi.org/10.1103/PhysRevLett.99.093904

Du J, Olhoff N (2007) Topological design of freely vibrating continuum structures for maximum values of simple and multiple eigenfrequencies and frequency gaps. Struct Multidisc Optim 34(2):91–110. https://doi.org/10.1007/s00158-007-0101-y

Gaynor A, Guest JK (2016) Topology optimization considering overhang constraints: eliminating sacrificial support material in additive manufacturing through design. Struct Multidisc Optim 54(5):1157–1172. https://doi.org/10.1007/s00158-016-1551-x

Gravesen J, Evgrafov A, Nguyen DM (2011) On the sensitivities of multiple eigenvalues. Struct Multidisc Optim 44(4):583–587. https://doi.org/10.1007/s00158-011-0644-9

Guest JK, Prevost JH (2006) Optimizing multifunctional materials: design of microstructures for maximized stiffness and fluid permeability. Int J Solids Struct 43:028–7047. https://doi.org/10.1016/j.ijsolstr.2006.03.001

Guest JK, Prévost JH (2007) Design of maximum permeability material structures. Comput Methods Appl Mech Eng 196(4–6):1006–1017. https://doi.org/10.1016/j.cma.2006.08.006

Hill R (1952) The elastic behaviour of a crystalline aggregate. Proc Phys Soc Sect A 65(5):349

Kao CY, Osher S, Yablonovitch E (2005) Maximizing band gaps in two-dimensional photonic crystals using level set methods. Appl Phys B 81(2):235–244. https://doi.org/10.1007/s00340-005-1877-3

Kube C (2016) Elastic anisotropy of crystals. AIP Adv 6:095209. https://doi.org/10.1063/1.4962996

Larsen UD, Sigmund O, Bouwsta S (1997) Design and fabrication of compliant micromechanisms and structures with negative poisson's ratio. J Microelectromech Syst 6(2):99–106. https://doi.org/10.1109/84.585787

Lazarov BS, Wang F, Sigmund O (2016) Length scale and manufacturability in density-based topology optimization. Arch Appl Mech 86(1):189–218. https://doi.org/10.1007/s00419-015-1106-4

Leary M, Merli L, Torti F, Mazur M, Brandt M (2014) Optimal topology for additive manufacture: A method for enabling

additive manufacture of support-free optimal structures. Mater Des 63:678–690. https://doi.org/10.1016/j.matdes.2014.06.015
Li Q, Chen W, Liu S, Tong L (2016) Structural topology optimization considering connectivity constraint. Struct Multidisc Optim 54(4):971–984. https://doi.org/10.1007/s00158-016-1459-5
Li Q, Chen W, Liu S, Fan H (2018) Topology optimization design of cast parts based on virtual temperature method. Comput Aided Des 94:28–40. https://doi.org/10.1016/j.cad.2017.08.002
Li W, Meng F, Chen Y, Li Y, Huang X (2019) Topology optimization of photonic and phononic crystals and metamaterials: A review. Adv Theory Simul 2(7):1900017. https://doi.org/10.1002/adts.201900017
Liu J, To AC (2017) Deposition path planning-integrated structural topology optimization for 3d additive manufacturing subject to self-support constraint. Comput Aided Des 91:27–45. https://doi.org/10.1016/j.cad.2017.05.003
Liu S, Li Q, Chen W, Tong L, Cheng G (2015) An identification method for enclosed voids restriction in manufacturability design for additive manufacturing structures. Front Mech Eng 10(2):126–137. https://doi.org/10.1007/s11465-015-0340-3
Men H, Lee KYK, Freund RM, Peraire J, Johnson SG (2014) Robust topology optimization of three-dimensional photonic-crystal band-gap structures. Opt Express 22(19):22632–22648. https://doi.org/10.1364/OE.22.022632
Men H, Nguyen NC, Freund RM, Parrilo PA, Peraire J (2010) Bandgap optimization of two-dimensional photonic crystals using semidefinite programming and subspace methods. J Comput Phys 229(10):3706–3725. https://doi.org/10.1016/j.jcp.2010.01.023
Meng F, Jia B, Huang X (2018) Topology-optimized 3d photonic structures with maximal omnidirectional bandgaps. Adv Theory Simul 1(12):1800122
Messner M (2016) Optimal lattice-structured materials. J Mech Phys Solids 96:162–183. https://doi.org/10.1016/j.jmps.2016.07.010
Moakher M, Norris AN (2006) The closest elastic tensor of arbitrary symmetry to an elasticity tensor of lower symmetry. J Elast 85(3):215–263. https://doi.org/10.1007/s10659-006-9082-0
Osanov M, Guest JK (2016) Topology optimization for architected materials design. Annu Rev Mater Res 46:211–233. https://doi.org/10.1146/annurev-matsci-070115-031826
Plocher J, Panesar A (2019) Review on design and structural optimisation in additive manufacturing: towards next-generation lightweight structures. Mater Des 183:108164. https://doi.org/10.1016/j.matdes.2019.108164
Qian X (2013) Topology optimization in b-spline space. Comput Methods Appl Mech Eng 265:15–35. https://doi.org/10.1016/j.cma.2013.06.001
Qian X (2016) Undercut and overhang angle control in topology optimization: a density gradient based integral approach. Int J Numer Methods Eng 111(3):247–272. https://doi.org/10.1002/nme.5461
Ranganathan SI, Ostoja-Starzewski M (2008) Universal elastic anisotropy index. Phys. Rev. Lett. 101(5):055504. https://doi.org/10.1103/PhysRevLett.101.055504
Sigmund O (1994) Materials with prescribed constitutive parameters: an inverse homogenization problem. Int J Solids Struct 31(17):2313–2329. https://doi.org/10.1016/0020-7683(94)90154-6
Sigmund O (1995) Tailoring materials with prescribed elastic properties. Mech Mater 20(4):351–368. https://doi.org/10.1016/0167-6636(94)00069-7
Sigmund O (2000) New class of extremal composites. J Mech Phys Solids 48(2):397–428. https://doi.org/10.1016/S0022-5096(99)00034-4
Sigmund O, Jensen JS (2003) Systematic design of phononic band-gap materials and structures by topology optimization. Philos Trans: Math Phys Eng Sci 361(1806):1001–1019. https://doi.org/10.1098/rsta.2003.1177
Sigmund O, Torquato S (1996) Composites with extremal thermal expansion coefficients. Appl Phys Lett 69(21):3203–3205. https://doi.org/10.1063/1.117961
Swartz KE, White DA, Tortorelli DA, James KA (2021) Topology optimization of 3d photonic crystals with complete bandgaps. Opt Express 29(14):22170–22191. https://doi.org/10.1364/OE.427702
Wang F, Jensen JS, Sigmund O (2011) Robust topology optimization of photonic crystal waveguides with tailored dispersion properties. J Opt Soc Am B 28(3):387–397. https://doi.org/10.1364/JOSAB.28.000387
Watts S, Tortorelli DA (2016) An n-material thresholding method for improving integerness of solutions in topology optimization. Int J Numer Methods Eng 108(12):1. https://doi.org/10.1002/nme.5265
Watts SE, Tortorelli DA (2017) A geometric projection method for designing three dimensional open lattices with inverse homogenization. Int J Numer Methods Eng 112(11):1564–1588. https://doi.org/10.1002/nme.5569
Wächter A, Biegler LT (2006) On the implementation of a primal-dual interior point filter line search algorithm for large-scale nonlinear programming. Math Program 106(1):25–57
Zhang K, Cheng G, Xu L (2019) Topology optimization considering overhang constraint in additive manufacturing. Comput Struct 212:86–100. https://doi.org/10.1016/j.compstruc.2018.10.011